Interactions of Fibroblast with Cytotoxic and Invasive Strains of *Pseudomonas aeruginosa* on ECM Mimicking Fibers

Lauren Berman

Thesis submitted to the faculty of the Virginia Polytechnic Institute and State University in partial fulfillment of the requirements for the degree of

Master of Science
In
Mechanical Engineering

Bahareh Behkam, Chair

Amrinder S. Nain

Sohan Kale

July 27, 2021
Blacksburg, VA

Keywords: mechanobiology, host cell-pathogen interaction, fibroblast, *pseudomonas aeruginosa*, extracellular matrix, nanofibers, wound infection

Interactions of Fibroblast with Cytotoxic and Invasive Strains of *Pseudomonas aeruginosa* on ECM Mimicking Fibers

Lauren Berman

Abstract (academic)

It is estimated that approximately 2 million fires which occur in United States each year result in 1.2 million burn victims. Fibroblasts are responsible for responding to this tissue damage by breaking down the damaged extracellular matrix (ECM) and secreting a new ECM which aids in wound repair and supports the migration of immune cells. *Pseudomonas aeruginosa* is an opportunistic pathogen commonly associated with health-care infections (HCAIs) due to its ability to take advantage of immunocompromised hosts. However, little research has investigated how wound invading *P. aeruginosa* interacts with wound repairing fibroblasts. To address this lack of understanding, this thesis focuses on quantifying changes in fibroblast morphology, migratory behavior, and force exertion to investigate this host cell's response to representative cytotoxic (PAO1) and invasive (PA14) strains of *P. aeruginosa.* These assays study host cell-pathogen interactions on highly aligned nanofibers of varied spacing and diameter, which mimic the fibroblast deposited ECM and dictate fibroblast morphology. We discovered that the cytotoxic strain of *P. aeruginosa* induced significantly shorter fibroblast death times. Furthermore, two modes of death, sharp and gradual, were identified and found to be dependent on both fiber configuration and strain of *P. aeruginosa*. In addition, fibroblasts exposed to PAO1 migrating on the parallel formation were found to be significantly slower and less persistent than those exposed to PA14, however, fibroblasts exposed to both strains of bacteria were shown to exert similar forces. Lastly, exposure to PA14 led to the greatest change in actin, evident by increased actin punctae and less prominent actin stress fiber formation.

Interactions of Fibroblast with Cytotoxic and Invasive Strains of *Pseudomonas aeruginosa* on ECM Mimicking Fibers

Lauren Berman

Abstract (general audience)

It is estimated that approximately 2 million fires which occur in United States each year result in 1.2 million burn victims. Fibroblasts respond to burn wounds by breaking down the damaged tissue fibers, termed extracellular matrix (ECM), and secreting a new ECM. Unfortunately, severe thermal injuries place hospitalized burn victims at high risk of infection. *Pseudomonas aeruginosa* is an opportunistic pathogen commonly associated with health-care infections (HCAIs) due to its ability to take advantage of immunocompromised hosts. However, little research has investigated how wound invading *P. aeruginosa* interacts with wound healing fibroblasts. To address this knowledge gap, this thesis focuses on quantifying changes in fibroblast shape, migratory behavior, and force exertion to investigate this host cell's response to two strains of *P. aeruginosa,* which employ different mechanisms of invasion. These interactions are studied on a platform of suspended nanofibers with controlled spacing and diameter, to dictate fibroblast shape and mimic the fibroblast deposited ECM. We discovered that the two strain of *P. aeruginosa* induced significantly different fibroblast death times. During death, it was observed that fibroblasts either balled up quickly, termed sharp death, or remained spread out, termed gradual death, dependent upon fibroblast shape and strain of *P. aeruginosa* introduced. In addition, significant differences in migration speed and persistence were found between fibroblasts exposed to the two strains of bacteria, however, both groups were shown to exert similar forces. Lastly, the fibrous proteins which make up the cytoskeleton of the cell, actin stress fibers, were found to vary among the control and bacteria treated cells.

Acknowledgements

Firstly, I would like to take the time to thank my graduate advisor, Dr. Bahareh Behkam. The enthusiasm she showed in class and in my undergraduate research opportunity is what led me to pursue a graduate degree. Throughout my research, she has always challenged me to try new and different approaches to solve problems, even if it resulted in failure and required further readjustments. I am extremely appreciative of the time Dr. Behkam has taken to brainstorm new experimental ideas with me and simply lend an ear when I was feeling overwhelmed. I would also like to thank Dr. Amrinder Nain for continuously supporting my research as a collaborator and a mentor. He consistently brought new perspectives to my research which introduced new experimental and analytical paths I had never thought of. Additionally, I would like to thank Dr. Sohan Kale for serving on my committee and providing insightful and critical comments that added clarity to my work.

I would also like to thank my family for being a constant source of support throughout my graduate endeavors. I am overwhelmed by the sacrifices my parents, Deborah and Matthew Robinson, have made to ensure I have a valuable education. I would also like to mention my grandparents, John and Kathryn Jones, who have always been my biggest cheerleaders. A special thanks to Ryan Hughes for his unwavering support and confidence in my success.

I owe a huge bout of gratitude to the current and past members of the MicroN BASE Laboratory and the STEP Laboratory for teaching me the ropes. I would specifically like to thank Apratim Mukherjee for his mentorship and unfaltering friendship. Thank you to Dr. Naimat Bari and Ying Zhan for helping me acquire SEM images of fiber networks and to Aldwin Pagulayan for

fabricating force scaffolds. Thank you to Nathanael High for helping me process raw data from my invasion experiments, your work was invaluable.

A special thanks to Dr. George O'Toole from the Department of Biological Sciences at Dartmouth College for providing us with the *Pseudomonas* strains critical for this study. Lastly, I would like to thank the Department of Mechanical Engineering for providing me with the Davenport Fellowship and Dr. Clinton Dancey for giving me the opportunity to be a graduate teaching assistant and supporting my graduate studies.

Table of Contents

List of Figures

Figure …….. Page Number

List of Tables

Chapter 1. Introduction

1.1 Motivation

Being the only organ exposed to environmental conditions, the skin proves to be most at risk to injuries such as cuts, scratches, and more severely, burns. In the event of tissue damage, chemoattractants are responsible for the migratory response of fibroblasts towards the wound clot (Tomasek et al. 2002). Subsequently, fibroblasts have three main tasks: to break down the damaged extracellular matrix (ECM), secrete a new ECM, and support the migration of additional cells that aid in wound repair and immune response. However, significant thermal injuries place burn victims in severe risk of immunosuppression, resulting in increased susceptibility to bacterial infection (Church et al. 2006). *Pseudomonas aeruginosa* is an opportunistic pathogen commonly responsible for hospital acquired infections where it may take advantage of immunosuppressed hosts, such as burn victims, by employing its various virulence factors (Driscoll, Brody, and Kollef 2007). However, despite fibroblasts being amongst the first responders to a wound site, the interactions between wound healing fibroblasts and wound invading bacteria, such as *P. aeruginosa*, is rarely studied.

In this thesis, we explored the interactions between two strains of *P. aeruginosa*, one invasive and one cytotoxic, and mouse embryo 3T3 fibroblasts. We quantified how the two strains, which employ various types and levels of virulence factors, affect fibroblast morphodynamics and contractility differently. These assays are performed on a platform of highly aligned suspended nanofibers which mimic the fibroblast deposited ECM. Manipulation of the fiber architecture (i.e., changing fiber spacing and diameter) introduced a new level of complexity by recapitulating the various morphologies fibroblasts take on in the depths of the dermis (Novotny and Gnoth 1991).

Ultimately, this fibrous platform could aid in the fundamental understanding of wound invasion *in vivo.*

1.2 Background

1.2.1 *Pseudomonas aeruginosa* and its Virulence Factors

Pseudomonas aeruginosa is a gram-negative, rod-shaped bacterium measuring about 0.5–1.0 μm in diameter and 1.5–5.0 μm in length. It is an opportunistic pathogen able to cause infections in immunocompromised hosts, most commonly in patients with cystic fibrosis (CF) or dermal infections. Significantly, *P. aeruginosa* is reported to be responsible for 11–13.8% of all hospital acquired infections (Driscoll, Brody, and Kollef 2007). Cited as a serious antibiotic resistance threat in the U.S. by the Center for Disease Control (CDC), *P. aeruginosa* is estimated to be responsible for $767 M in healthcare costs and 32,600 infections in hospitalized patients, 2,700 of which have resulted in mortality (CDC 2019). It is known to be a particularly dangerous pathogen due to its many virulence factors and mechanisms of antimicrobial resistance.

Flagella. *P. aeruginosa* produces a single polar flagellum which measures about 2.5 wave units in length, each wave having a contour (wavelength) of 1.8 μm (Dasgupta, Arora, and Ramphal 2004). As seen in Figure 1.1, the flagellum consists of three major components which work together to promote swimming motility: the filament, the hook, and the basal body. The basal body is associated with a motor/switch which is responsible for the clockwise or counterclockwise rotation of the filament, allowing *P. aeruginosa* to swim backwards and forwards, respectively, leading to the random walk motion of the bacterium (Vater et al. 2014). Furthermore, chemoreceptors on the bacterial surface called methyl accepting chemotaxis proteins (MCPs) are able to intercept chemotactic signals in the form of environmental attractants and repellents to regulate a series of Che proteins which communicate with the flagellar motor (Kato et al. 2008).

In response, the flagellar motor can spin filaments at speeds upwards of 15,000 rpm, aiding in bacterial motility and providing sufficient force to propel bacteria away from a chemorepellent or towards a chemoattractant, such as a host cell surface (Magariyama et al. 1994). Finally, on the end of the filament is a capping protein, FilD, which has been shown to be responsible for *P. aeruginosa* adhesion to human mucins (Arora et al. 1998).

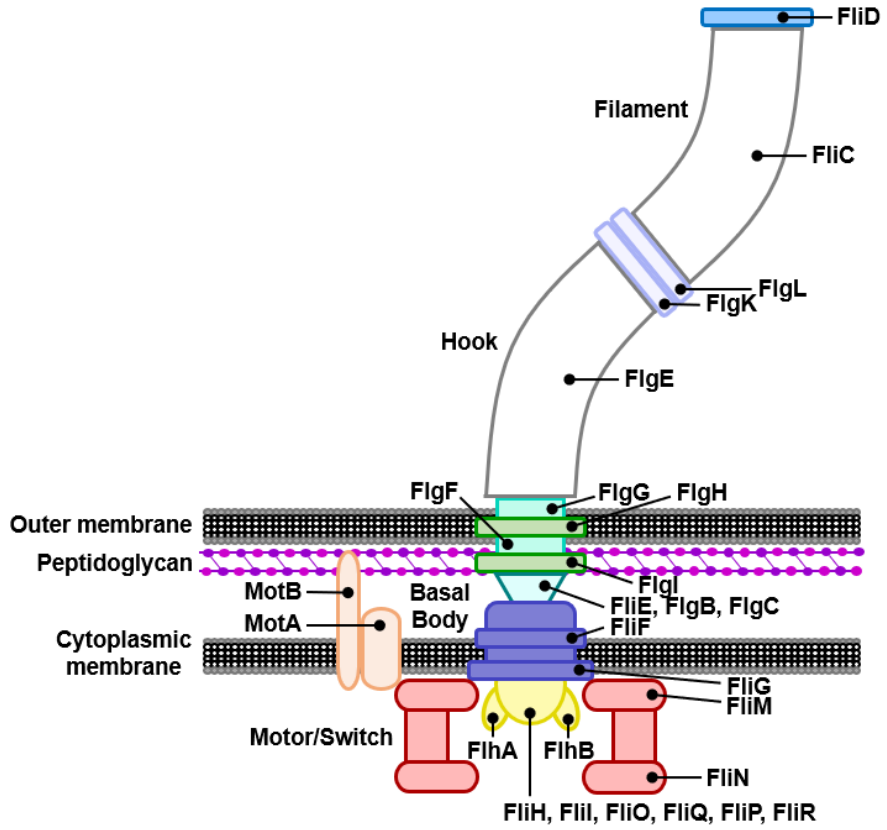

Figure 1.1. The flagellum consists of three major components which work together to promote motility: the filament, hook, and basal body. *P. aeruginosa* is characterized by a single polar flagellum which modulates its speed and directionality dictated by chemotactic signals in the environment.

Recently, research has shown that the role of bacteria flagella may go beyond motility and surface adhesion. A study of *P. aeruginosa* flagella-dependent activation of airway epithelial cell receptors and signaling pathways revealed production of neutrophil chemotactic factors and pro-inflammatory cytokines interleukin 6 (IL-6) and IL-8 as a response to flagellar binding to

asialoGM1, toll-like receptor 2 (TLR-2), and toll-like receptor 5 (TLR-5) in a variety of human epithelial cells. This study demonstrated the flagellar role in the induction of inflammatory responses and early immune responses (Adamo et al. 2004). In another study, the absence of FliC, a flagellin protein which makes up the flagella filament, resulted in no mouse mortality as compared to 30% mortality caused by parent strain PAK which retained the FliC protein (Feldman et al. 1998). In addition, only 25% of the mice inoculated with the *fliC* mutant experienced pneumatic symptoms whereas 80% of mice inoculated with the parent strain were confirmed to develop pneumatic infection. Histopathological studies showed that *fliC* mutants were not able to elicit a widespread inflammatory response, instead causing minor localized inflammation in the lungs. Although the exact role the flagella plays in cell death is still poorly understood, it is evident that the flagella is at the very least, critical for propelling *P. aeruginosa* to the host cell surface to employ other contact dependent virulence factors.

Type IV pili. Type IV pili (TFP) were first reported on the poles of *P. aeruginosa* in the 1970s (Bradley 1972). TFP are hair-like filaments typically 4 μm long and 5-6 nm in diameter (Craig, Forest, and Maier 2019). As depicted in Figure 1.2, the TFP of *P. aeruginosa* are comprised of four main components: two ATPase complexes, a platform protein, a secretin channel, and a pilus filament.

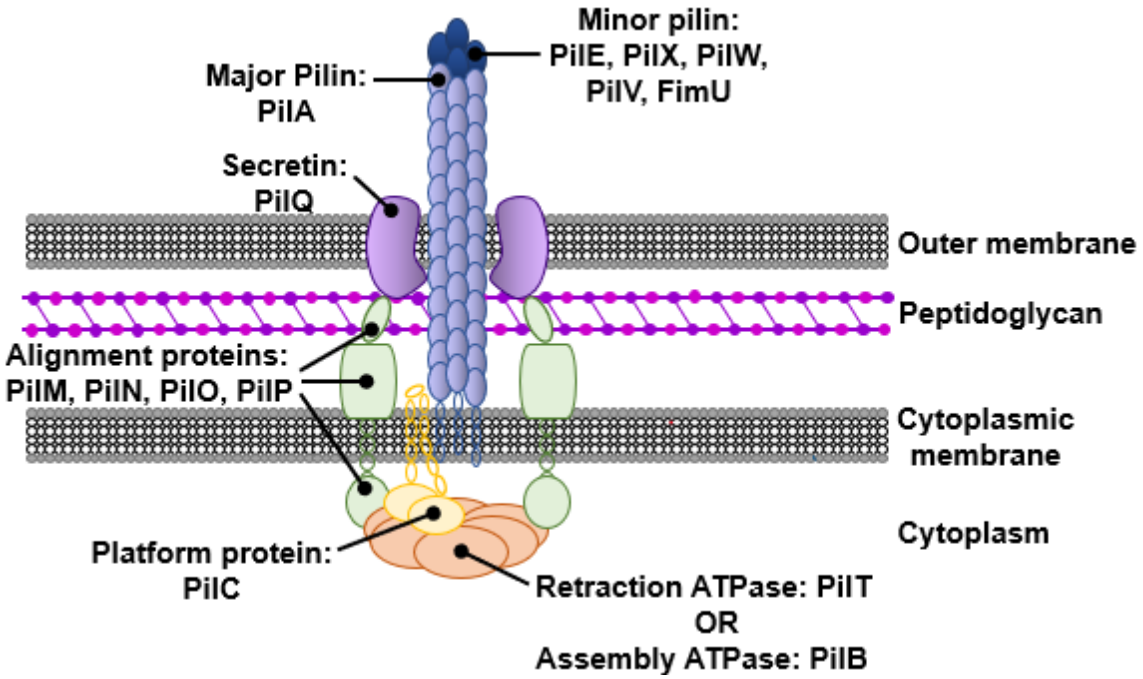

Figure 1.2. Type IV pili are made up of four main components (two ATPase complex, platform protein, secretin channel, and pilus filament) which work in tandem to drive pilus assembly and disassembly. The continuous extension and retraction of pili results in the twitching motion that characterizes *P. aeruginosa* surface motility.

The extension (PilB) and retraction (PilT) ATPase proteins located in the cytoplasm work in sequence to drive pilus polymerization and depolymerization. Cyclic extension and retraction of TFP allow the bacterium to attach to and migrate on the surface of eukaryotic host cells and other solid surfaces. Specifically, small pilin proteins that comprise the fimbriae are thought to be the contributor to adhesion (Paranchych and Frost 1988). At the end of the pilus shaft is an adhesive tip structure having a shape corresponding to that of specific receptors on a host cell. Previous studies have stated that asialo-GM1 serves as the epithelial cell receptor for the binding of *P. aeruginosa* pili by employing indirect techniques, such as inhibition of binding by anti-GM1 antibodies; however, more recent studies have contradicted this claim by investigating the glycolipid-binding specificity of laboratory and clinical *P. aeruginosa* strains (Comolli et al. 1999; Emam et al. 2006). The inner membrane platform protein (PilC) works in tandem with the ATPase

complexes to build upon or deconstruct the pilus filament one pilin unit at a time through the outer-membrane secretin channel comprised of PilQ proteins.

The primary function of TFP is thought to be "twitching motility" which allows bacteria to translocate across solid surfaces (Mattick, Whitchurch, and Alm 1996). First termed by Lautrop in 1961, twitching motility is a flagellum-independent motion that appears as sudden sharp changes in direction of motion at speeds up to 0.1 μm s^{-1} on abiotic surfaces (Lautrop 1962; Semmler, Whitchurch, and Mattick 1999). Twitching motility is caused by repeated extension, attachment, and retraction of TFP as described previously. *P. aeruginosa* exploits this twitching motility for initial attachment to hosts; thus, TFP are necessary to employ contact dependent virulence factors. In fact, it was shown through the use of *P. aeruginosa* pili mutants that twitching motility is necessary for *P. aeruginosa* to migrate beneath the epithelial cell layer while TFP are necessary for binding to the apical surface of a polarized epithelium (Golovkine et al. 2016; Bucior, Pielage, and Engel 2012). Therefore, TFP have been proven to be a crucial virulence factor for *P. aeruginosa* invasion.

Secretion systems. Bacteria have evolved a wide array of machinery used to transport various virulence factors across the bacterial envelope. So far, six types of secretion systems have been identified in Gram-negative bacteria, five of which are employed by *P. aeruginosa* (Costa et al. 2015; Wu et al. 2015). These secretion systems can be separated into two categories, those which eject proteins directly into a host cell membrane (Types III, VI) and those which eject proteins into the environment (Types I, II, V).

Critical to *P. aeruginosa* contact dependent virulence is the type III secretion system (T3SS) which works to inject toxins directly into the host cell, requiring bacteria-host cell contact. The T3SS can

be divided into five components shown in Figure 1.3: the needle complex, the translocation apparatus, regulatory proteins, chaperone proteins, and effector proteins (Hauser 2009).

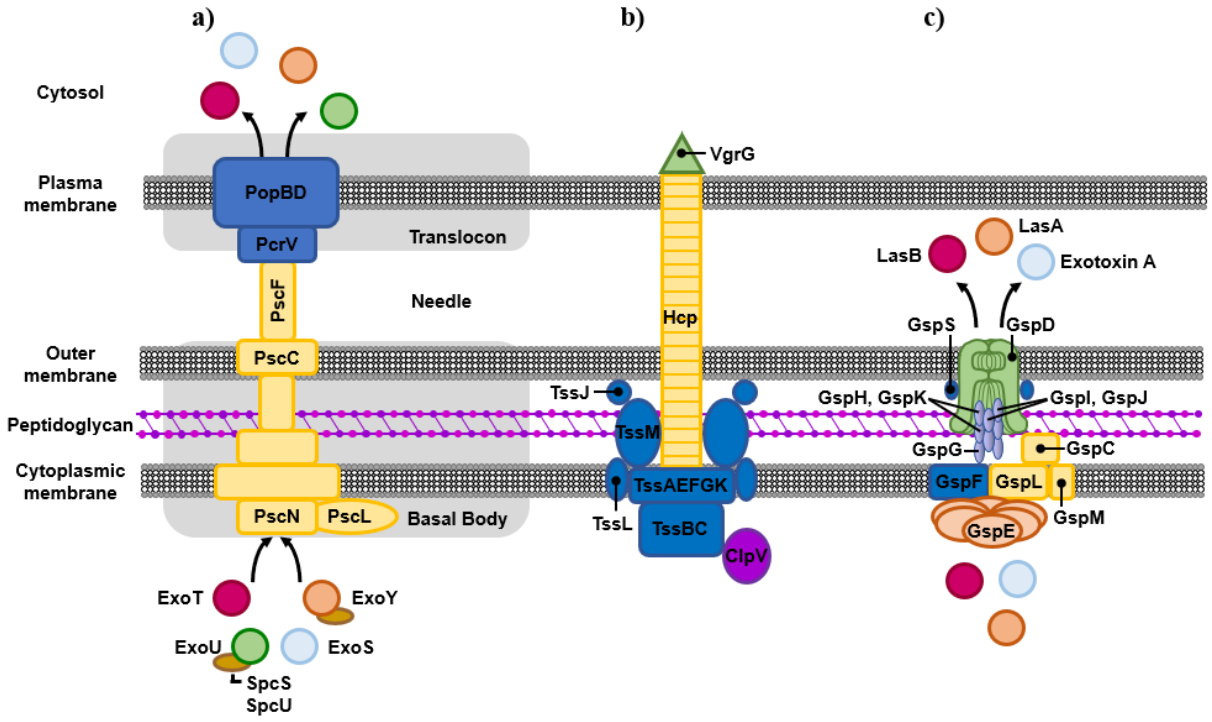

Figure 1.3. The a) type III and b) type VI secretion systems are the two secretion systems employed by *P. aeruginosa* which inject toxic proteins directly into a host cell across the two bacterial membranes and eukaryotic cell membrane. The c) type II secretion system releases toxic proteins into the extracellular environment across both bacterial membranes.

The needle complex is comprised of subunits of the protein PscF (Pastor et al. 2005). This structure serves to both detect the cell membrane as well as allow the transport of secretion proteins across both bacterial membranes and the thin layer of peptidoglycan. The translocation apparatus forms a membrane pore that receives and delivers effector proteins secreted by the needle complex (Hauser 2009). This apparatus provides the effector proteins with a direct route across the host membrane and into its cytosol. *P. aeruginosa* specific translocator proteins PopB and PopD collaborate to form the membrane pore estimated to be 2.8–3.5 nm in diameter (Dacheux et al. 2001). This pore allows for the secretion of effectors directly into the host cytoplasm. Prior to

secretion, however, chaperone proteins bind to effector proteins to ensure proper delivery through the translocation apparatus (Hauser 2009). Thus far, four effector proteins have been identified in the *P. aeruginosa* T3SS: ExoS, ExoT, ExoU, and ExoY (Yahr et al. 1998). Of note, ExoS and ExoT play a particularly important role in targeting mammalian cell signaling complexes which control cell proliferation, migration, and survival, which will be discussed in further detail below. More recently discovered, the T6SS is also responsible for injecting proteins directly into a variety of cells, including eukaryotic hosts as well as other bacteria, depending on the type of T6SS employed (Green and Mecsas 2016). For example, of the three types of T6SSs discovered in *P. aeruginosa* thus far, HSI-I works to target other bacteria for the purpose of environmental competition (Russell et al. 2011). By contrast, the HSI-II has been shown to promote internalization in epithelial cells by rearranging complexes in the host cytoskeleton, which will be discussed in more depth in a following section (Thibault G. Sana et al. 2015). Currently, the function of the HSI-III T6SS is unknown.

Of the contact-dependent secretion systems, the T2SS arguably plays the greatest role in *P. aeruginosa* virulence (Moradali, Ghods, and Rehm 2017). The T2SS relies on a two-step secretion process: Sec- or Tat- dependent secretion into the periplasm, followed by T2SS dependent secretion into the extracellular environment (Wu et al. 2015). T2SS complex-mediated secretion involves the use of four components: the outer-membrane complex, the inner-membrane platform, the secretion ATPase, and the pseudopilus (Korotkov, Sandkvist, and Hol 2012). Comprised of secretin proteins, the outer-membrane complex is responsible for the transport of folded proteins through the outer membrane, connected to the periplasm through the inner membrane platform. Due to its contact with the secretin, pseudopilus, and ATPase, the inner membrane platform plays a crucial role in coordinating the secretion of proteins from the periplasm through the outer

membrane platform. Similar to the ATPase which powers pilus assembly and disassembly, the secretion ATPase, which resides in the cytoplasm, is responsible for providing energy to the T2SS. Interestingly, the pseudopilus has evolutionary ties to the pilin proteins which comprise the type IV pili (Figure 1.2), however its exact role in the T2SS remains unknown (Sauvonnet et al. 2000). Overall, these four components work together to secrete a variety of key virulence mediated proteins into the extracellular environment including exotoxin A and elastases LasA and LasB (Moradali, Ghods, and Rehm 2017). The specific role of these virulence proteins in bacterial colonization will be delved into in a coming section.

Like the T2SS, the T5SS relies on a two-step secretion process to secrete virulent proteins such as EstA, LepA, and LepB into the environment (Wu et al. 2015). Lastly, the TISS is responsible for the secretion of the alkaline protease AprA into the environment, which cleaves a variety of proteins including laminin, interferon, tumor necrosis factor-α, and interleukin-6 (Hoge et al. 2010). Overall, the T1SS impedes the host immune response, critical for early stages of wound infection.

Interestingly, *P. aeruginosa* isolates have also been differentiated into two groups, phenotypically invasive or cytotoxic (Fleiszig et al. 1996). In this paper, ten corneal and four noncorneal *P. aeruginosa* isolates were assessed for their ability to induce cytotoxicity and enter epithelial cells as quantified by chromium release and gentamicin survival assays, respectively. An inverse correlation was found between the ability of *P. aeruginosa* isolates to induce cytotoxicity and invade epithelial cells; none of the cytotoxic isolates were capable of invasion and all non-cytotoxic isolates could be identified intracellularly. Recently, it has also been suggested that the phenotype displayed may correlate with the types and levels of secretion systems employed during *P. aeruginosa* colonization (Fleiszig et al. 1997). For example, the same authors from the

previously discussed study showed that when screening for complements of *exoS and exoT* (exoenzymes secreted by the T3SS), all cytotoxic and invasive strains maintained the complement for *exoT* but only the invasive strains maintained the complement for *exoS.* This result led authors to conclude that the cytotoxic strains of *P. aeruginosa* had acquired a mutation in the *ladS* gene, resulting in differential activity of the T3SS as compared to invasive strains. Another study analyzed the partial genome of *P. aeruginosa* strains PA14 and PAO1, strain PA14 known for being particularly virulent (T. G. Sana et al. 2021). It was found that 2,029 genes were differentially expressed between the two strains, including an anti-quorum sensing regulator, *qslA*, expressed in high levels in PAO1 and low levels in PA14. Authors hypothesized that the low levels of *qslA* expression in PA14 may be correlated with its high cytotoxicity due to its ability to better detect bacterial population density and respond through virulent gene regulation. Consequently, this thesis will delve further into the differing effects that colonization of cytotoxic (PA14) and invasive (PAO1) strains of *P. aeruginosa* have on fibroblast morphodynamics and contractile force regulation.

1.2.2 Fibroblast Migration and Their Role in Wound Healing

Fibroblasts are a member of the connective-tissue cell family, cells that play a critical role in the foundation and repair of tissues and organs (Alberts et al. 2014). Specifically, fibroblasts secrete collagen extracellular matrix (ECM) which provides structural support for fibroblast migration and the recruitment of immune response cells in the event of wound formation.

***Mesenchymal migration*.** On a molecular level, cell-ECM interactions are facilitated by *integrins,* a transmembrane protein that transmits information about the surrounding environment to the inside of the cell. Integrins also play a key role in establishing focal adhesions which link actin,

one of the three major cytoskeletal components, to ECM proteins such as collagen, fibronectin, and laminin (Alberts et al. 2014). More specifically, as integrins bind to the extracellular matrix, they cluster in the membrane, forming focal adhesions, and associate with a signaling complexes which promotes actin formation. In turn, stress fibers, otherwise known as actin-protein complexes, promote addition integrin clustering, bolstering extracellular matrix adhesions.

Eukaryotic cell locomotion can be broken down into four steps pictured in Figure 1.4: protrusion, attachment, translocation, and release (Jacobs, Huang, and Kwon 2012). Each of these steps can be performed simultaneously and require constant rearrangement and formation of actin filaments and focal adhesions. Protrusions occur when the cell extends actin-abundant protuberances in the direction of desired movement. These protuberances can be classified as lamellipodia or filopodia when migration occurs on 2D surfaces or 3D nonlinear elastic surfaces, such as collagen. In 1970, Abercrombie *et al.* published five successive papers which ultimately derived the classical model of lamellipodia-dependent cell migration (Abercrombie, Heaysman, and Pegrum 1971). Lamellipodia can be described as flat, wide extensions consisting of highly branched actin networks at the leading edge of migratory cells, whereas filopodia are long, thin extensions containing cross-linked actin clusters (Jacobs, Huang, and Kwon 2012). By contrast, protuberances on 3D linear elastic surfaces are classified as lobopodia (Petrie et al. 2012). First discovered by introducing fibroblasts on dermal explants and cell derived matrices, lobopodia are blunt ended protrusions with blebs projecting to the side. Unlike lamellipodia, lobopodia are formed by actomyosin contractile-driven pressure rather than by actin clusters. In order to migrate, cells must simultaneously form focal adhesions to secure the cell to the extracellular matrix and release focal adhesions at the trail end of the cell during retraction. As a result, translocation will occur in the direction of which new focal adhesions are forming.

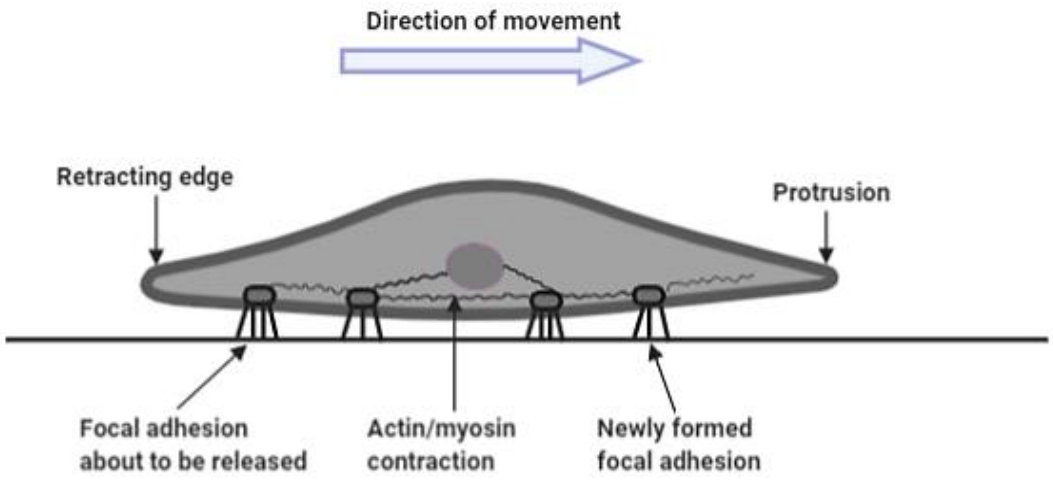

Figure 1.4. Four main steps characterize the migration of eukaryotic cells. The cell extends a protrusion in the direction of motion and anchors it through newly established focal adhesions. Simultaneously, the cell undergoes translocation by means of actomyosin contraction while releasing focal adhesions on its trail end.

Fibroblast Morphology. *In vivo* fibroblast morphology has been shown to vary depending on its location in the depths of the dermis (Novotny and Gnoth 1991). Using a silver impregnation technique, authors were able to visualize fibroblasts in paraffin serial sections (Novotny and Gommert-Novotny 1990). With this visualization technique, authors proved a relationship between the collagen architecture of the connective tissue and fibroblast morphology (Novotny and Gnoth 1991). Figure 1.5 shows images of fibroblasts in various layers of the papillary dermis. Fibroblasts in the subepidermal band had elongated bodies with long, thick protrusions running directly parallel to the epidermis (Figure 1.5b). By contrast, fibroblasts in the layer directly below the subepidermal band had more circular morphologies (Figure 1.5c). It was also observed that towards the reticular dermis the cell spread area gradually increased.

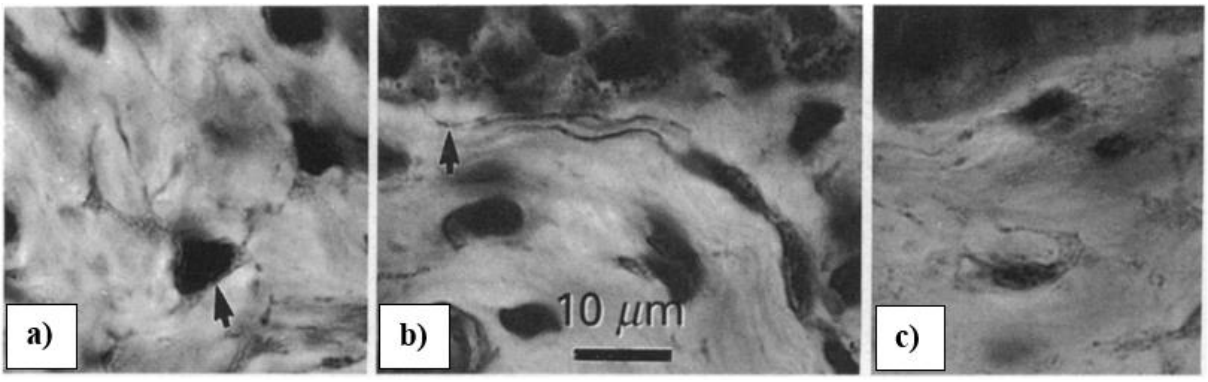

Figure 1.5. Images were taken of fibroblasts of varied morphologies in layers of the papillary dermis: a) Stellate fibroblasts with protrusions joining those of neighboring cells, b) elongated fibroblasts in the subepidermal band of the papillary dermis with long protrusions running parallel to the epidermis, and c) fibroblasts directly below the subepidermal band, taking on curved morphologies (Novotny and Gnoth 1991).

While studies of cell migration in 3D environments more accurately recapitulate *in vivo* conditions, there are challenges associated with recreating and imaging the precise structure of the 3D ECM *in vitro.* Accordingly, researchers have used a reductionist approach to 3D cell migration by means of 1D topography, in hopes of discovering common mechanisms of migration. In one study, microphotopatterning was used to highlight similar migration speeds, uniaxial movement, and dependence on myosin contractility in both 3D and 1D migration, characteristics which differ from those of 2D migration (Doyle et al. 2009). Thus, it has been proposed that 3D migration can be adequately described using a 1D migration model. Accordingly, this thesis will utilize a reductionist approach by means of a 1D fibrous migration platform to quantify fibroblast migration parameters.

Wound repair. In the event of tissue damage, a fibrin clot first covers up the exposed wound (Figure 1.6) (Tomasek et al. 2002). Subsequently, chemoattractants, such as platelet-derived growth factor (PDGF), secreted by platelets embedded within the clot, stimulate a chemotactic migratory response of fibroblasts towards the wound. Fibroblasts appear at the wound site 24-48 hours post-injury, at the beginning of the proliferative phase (i.e., the wound repair phase wherein

fibroblast begins to secrete ECM), and use matrix metalloproteinases (MMPs) to break down the damaged clot ECM, composed of polysaccharide chains of glycosaminoglycans and fibrous proteins (Forrest 1983; Alberts et al. 2014). Subsequently, fibroblasts replace the clot with a new collagenous ECM to support the migration of innate immune cells, such as neutrophils and macrophages, which aid in wound repair and infection prevention. Lastly, fibroblasts aid in closing the wound by exerting contractile forces on the deposited ECM.

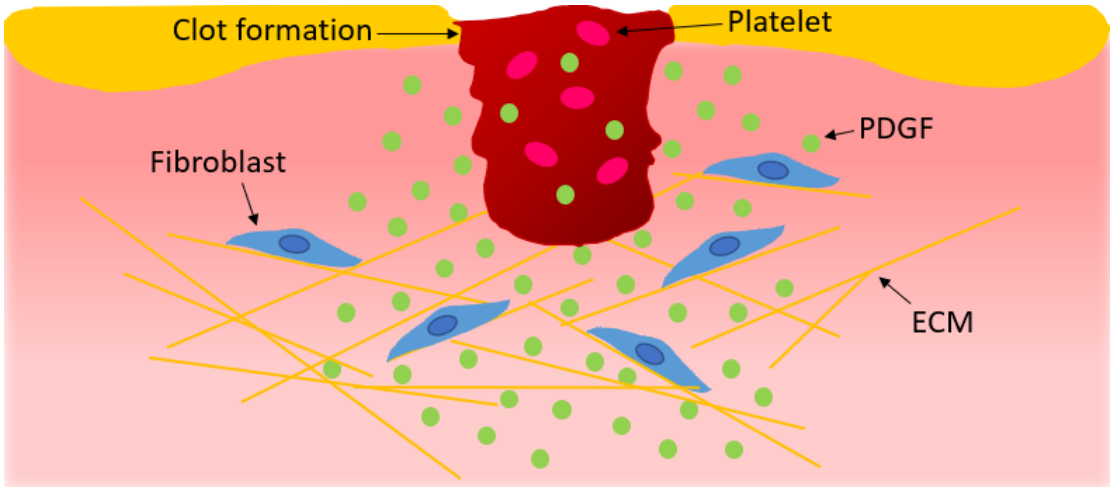

Figure 1.6. In the event of a wound, fibroblasts exhibit a migratory response to growth factors released by platelets embedded within the wound. At the wound site, fibroblast break down the damaged ECM, deposit a new ECM, and recruit other cells to aid in immune response.

All chronic wounds are occupied by microbes, however, some microbial wound infection can be detrimental. In particular, wound infections present a challenge to hospitalized burn victims who may suffer from immunosuppression as a result of severe thermal injuries (Driscoll, Brody, and Kollef 2007). Data gathered from the National Center for Injury Prevention and Control estimate that approximately 2 million fires which occur in United States each year result in 1.2 million victims with burn wounds (Church et al. 2006). A mature biofilm developed in the wound of a burn victim can act as a barrier against antimicrobial activity and the host immune system. An *in vitro* experiment using biopsied human skin isolated from a burn victim showed that *P. aeruginosa* was able to develop a mature biofilm in 10 hours (Harrison-Balestra et al. 2003). Once colonized,

P. aeruginosa has also been shown to secrete a variety of proteinases such as elastase, which aids in degrading necessary extracellular products such as elastin and fibrin (Morihara et al. 1965). In an *ex vivo* wound healing assay, *P. aeruginosa* was shown to degrade extracellular matrix proteins, such as fibroblast extracellular proteins, ^{35}S-methionine and ^{35}S-sulphate, purified human fibronectin, and decorin (Schmidtchen et al. 2003). This introduces a significant barrier for wound healing fibroblasts, for example, whose migration relies on the cell-binding domains of extracellular matrices provided by matrix adhesion proteins such as fibronectin (Missirlis et al. 2017). In addition, the degradation of extracellular matrix proteins may stunt the migration of immune cells that rely on fibroblast deposited extracellular matrices to respond to the threat of wound infection. An additional study demonstrated that elastase-producing *P. aeruginosa* were not only able to stunt fibroblast cell migration through the degradation of ECM proteins, but inhibit fibroblast growth (Schmidtchen et al. 2003). Another *P. aeruginosa* virulence factor, pyocyanin, has been shown to inhibit wound repair by inducing premature cellular senescence (Muller, Li, and Maitz 2009). In this study, wound dressings from burn victims were assessed for levels of pyocyanin so human diploid fibroblasts (HDFs) could be treated with the equivalent concentrations. As a result, all fibroblasts treated with pyocyanin ceased to grow and expressed increased levels of β-galactosidase, a biomarker of cellular senescence. Ultimately, as treatment with a p38^{MAPK} inhibitor allowed for continued replication and typical morphological characteristics, it was shows that pyocyanin targeted the Erk/p38^{MAPK} pathway previously shown to be activated by a variety of environmental stresses (Iwasa, Han, and Ishikawa 2003). These studies demonstrate the critical need for additional investigation into bacteria-fibroblast interactions.

1.2.3 *Pseudomonas* Interaction with Host Cells

Pseudomonas aeruginosa uses countless virulence factors to colonize host cells, many of which have yet to be fully investigated and perhaps many more yet to be discovered. However, it is also vital to understand how these virulence factors interact with the host cell, and which parts of the cell they target for the best invasion results. A recent study showed that treatment of *P. aeruginosa* virulence factor and carbohydrate-binding protein, LecB, on the basolateral surface of epithelial cells resulted in the disappearance of tight cell junctions and an increase in morphological circularity (Thuenauer et al. 2020). LecB was shown to interact with β1-integrins on the basolateral surface of cells, causing integrin endocytosis. As a result, *P. aeruginosa* invasive strain PAO1 was able to weaken cells-surface adhesion to crawl underneath cells, whereas the LecB deficient mutant inhibited this action. Another study revealed a paracellular route of transmigration of *P. aeruginosa* strains CHA and PAK across epithelial cell monolayers (Golovkine et al. 2016). Transmigration events were most commonly seen at sites of cell-cell junctions, cell division, or when elder cells were discharged from the monolayer. During these events, *P. aeruginosa* exploited discontinuities in the monolayer to gain access to the basolateral surface, first by one bacterium, then followed by a swarm of additional bacteria.

Arguably, the types of secretion systems employed by *P. aeruginosa* have the most profound effect on colonization. For example, as alluded to above, the proteins secreted by the T3SS directly into the host cell work to interfere with Ras-mediated signal transduction (Barbieri and Sun 2004). This pathway, also known as the MAPK pathway, is a series of proteins facilitating communication between the nucleus and cytoskeletal receptors. The presence of GTPase activating proteins of cytotoxins ExoS and ExoT on the surface of mammalian cells resulted in the disruption of the actin cytoskeleton, incapacitating the host response to migration, growth, differentiation, and survival,

ultimately inducing apoptosis. Another contact-dependent secretion system which was found to interfere with the host cytoskeletal arrangement is the T6SS. The HSI-II T6SS was shown to promote *P. aeruginosa* PAO1 internalization in epithelial cells through modulation of host microtubules (Thibault G. Sana et al. 2015). In this study, it was shown that the HSI-II T6SS secreted effector protein VgrG2b interacted with the γ-tubulin ring complex (γTuRC) responsible for catalyzing microtubule nucleation. Using two microtubule-destabilizing drugs, this interaction was shown to be key in mediating *P. aeruginosa* internalization, evident by the absence of VgrG2b-mediated entry. Of the contact independent secretion systems, the T2SS has been shown to be responsible for the release of various virulence factors that interact with host and extracellular matrix proteins, namely exotoxin A and elastases LasA and LasB. A particular study compared the ability of the secretome of the LasB-expressing and Las-B deficient (Δ*lasB)* PAO1 strains to induce apoptosis of endothelial cells and proteolyze cell-matrix adhesions (Beaufort et al. 2013). It was found that the LasB-deficient strain had no significant impact on endothelial cell viability whereas the LasB-expressing strain induced endothelial apoptosis. In addition, analysis from immunofluorescent microscopy revealed a quick decrease in immunolabeled fibronectin and von Willebrand factor when endothelial cells were exposed to the LasB-expressing PAO1 strain. Arguably the most toxic extracellular protein secreted by *P. aeruginosa,* exotoxin A, is responsible for inhibiting protein synthesis by the ADP-ribosylation of cellular elongation factor 2, ultimately inducing cell apoptosis (Michalska and Wolf 2015). In fact, in a mouse model, exotoxin A-producing strains have shown a 20-fold increase in virulence compared with exotoxin A-deficient mutants (Miyazaki et al. 1995).

While many studies have investigated how *P. aeruginosa* utilizes its virulence factors to exploit the epithelial monolayer, few studies have explored single-cell interactions between *P. aeruginosa*

and fibroblasts. This thesis will elucidate the importance of studying these interactions by characterizing the temporal changes in fibroblast morphodynamics and contractility in response to interaction with cytotoxic and invasive strains of *P. aeruginosa*.

1.3 Objectives and Organization of the Thesis

The overall goal of this thesis is to quantitatively investigate the spatiotemporal dynamics of fibroblast morphology, migration, and force exertion over the course of invasion by representative cytotoxic and invasive strains of *Pseudomonas aeruginosa*. To recapitulate the various fibroblast morphologies seen within dermal layers, we have utilized a nanofiber manufacturing platform that yields ECM-mimicking networks of suspended nanofibers ranging in spacing (5-50 μm) and diameter (550 nm – 2 μm). Furthermore, we added an additional complexity by introducing two strains of *P. aeruginosa*, one cytotoxic and one invasive, to gauge if 1) fibroblast morphology influences susceptibility to bacterial invasion and 2) whether the two bacteria strains elicit differing fibroblast response to invasion. We hypothesized that both fiber network configuration and bacteria strain will influence fibroblast morphodynamics and contractile force regulation. To test our hypothesizes, this thesis aimed to quantitatively study the effects of nanofiber geometry and strain of *P. aeruginosa* on fibroblast death time, morphology change, migration rate, force exertion, and actin structure. The remainder of this thesis is organized as follows:

Chapter 2: This chapter details the experimental and analysis methods for the study of *P. aeruginosa*- fibroblast interactions on ECM-mimicking fibers. Parameters for the fabrication of three types of nanofiber scaffolds are discussed and details of biological assays on nanofibers are described. Additionally, we report the imaging and analysis methods and numerical parameters

used to identify the effects of fiber network configuration and bacteria strain on the morphodynamic and force regulation of 3T3 fibroblasts.

Chapter 3: This chapter illustrates the results for the study of mouse embryonic fibroblast NIH/3T3 response to invasion by *P. aeruginosa* strains PA14 and PAO1. Invasion response was obtained by quantifying the following parameters: time of death, and temporal evolution of spread area, circularity, migration, and force. Immunofluorescence microscopy was used to qualitatively compare the actin structures in control and bacteria-treated cells. Experimental results are followed by a discussion on how our fibrous platform facilitates meaningful fibroblast-ECM and fibroblast-bacteria interactions.

Chapter 4: This chapter summarizes the key contributions of this thesis and discusses conclusions drawn from the findings. This section also underscores the importance of this work to the scientific community as well as the limitations of the current study that highlight potential future directions for fibroblast invasion assays.

Chapter 2. ECM-Mimicking Suspended Nanofibers for Physiologically Relevant Investigation of Host Cell-Pathogen Interaction

2.1 Fibrous Scaffold Fabrication

Suspended nanofibers were deposited on biocompatible hollow 316 stainless steel scaffolds using the Spinneret based Tunable Engineered Parameters (STEP) technique. The STEP platform is a non-electrospinning technique that deposits highly aligned fibers of specified diameter and spacing, as shown in Figure 2.1 (Nain et al. 2009). Through the force of a plunged syringe, a polystyrene solution (molecular weight: 2×10^6 g/mol) was propelled through tubing and a micropipette cut to a specified diameter, forming a droplet at the tip of the pipette. Simultaneously, a substrate holder which grasped the substrate from the stub, leaving the scaffold area completely exposed, was spun by a motor at a user defined rotational speed, and the micropipette was placed in proximity to the scaffold to form a continuous polystyrene fiber around the substrate. Subsequently, the positioning stage was moved translationally at a user defined speed, so the fiber wrapped around the length of the substrate with a spacing in correspondence with the translational speed. After the first layer was deposited, the substrate was turned 90 degrees and clasped by the other end of the stub by the substrate holder. The spinning process was repeated so that a second layer of fibers was deposited perpendicular to the previous, as needed. Three different fiber configurations were achieved using the STEP technique and are described in more detail below.

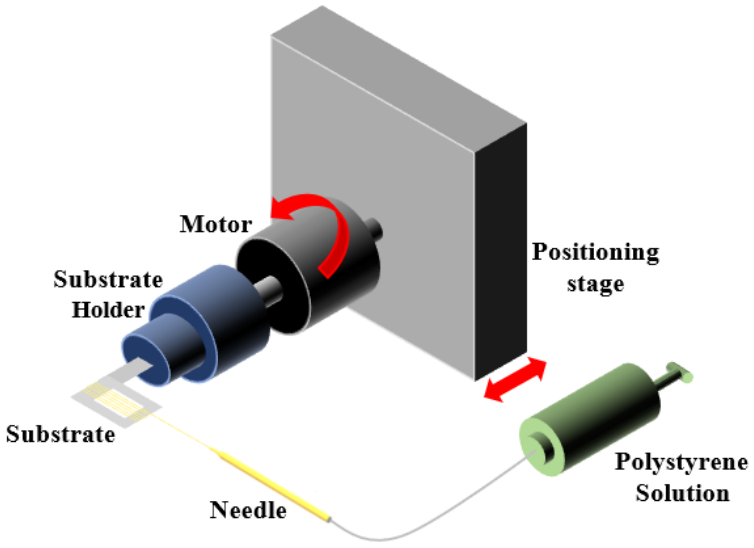

Figure 2.1. The STEP platform was used to deposit aligned nanofibers with specified spacing and diameter. A polystyrene solution was pushed through a needle and placed in contact with a rotating scaffold, forming a continuous fiber. Next, a translational speed was prescribed to the stage which allowed the fiber to wrap around the length of the scaffold.

Crosshatch fibrous scaffolds of 556 ± 55 nm diameter were fabricated using a 10% polystyrene in xylene solution. Three spacings were achieved by maintaining a constant rotational speed and varying the translational speed for each third of the scaffold length. This process was identically repeated perpendicular to the first layer to produce three different rectangular meshes on the scaffold diagonal, as seen in Figure 2.2a. These three speeds resulted in scaffold spacings of 5.0 ± 0.9 μm, 18.8 ± 1.7 μm, and 48.2 ± 2.8 μm, respectively. Throughout this thesis, these crosshatch spacings will termed 5, 20, and 50 μm, respectively.

Parallel fibrous scaffolds of 534 ± 115 nm diameter were also fabricated using a 10% polystyrene in xylene solution. Two different spacings were achieved for migration scaffolds by maintaining a constant rotational speed and varying the translational speed halfway through the scaffold. These two speeds resulted in scaffold spacings of 26.3 ± 3.0 μm and 14.1 ± 2.6 μm, respectively. Throughout this thesis, these migration configurations will be termed parallel (25) and parallel (15), respectively. Fibers were also deposited on both ends of the scaffold, perpendicular to the

migration fibers, to provide additional support. A diagram of the fibrous migration scaffold is shown in Figure 2.2b. Lastly, force scaffolds were constructed by depositing parallel base fibers 2.2 ± 0.3 μm in diameter. A second layer of parallel fibers at 195 ± 28 nm diameter and 7.5 ± 1.8 μm spacing was deposited perpendicular to the base fibers to provide fixed-fixed boundary conditions and facilitate accurate force quantitation, as described in more detail below. A force scaffold diagram is depicted in Figure 2.2c.

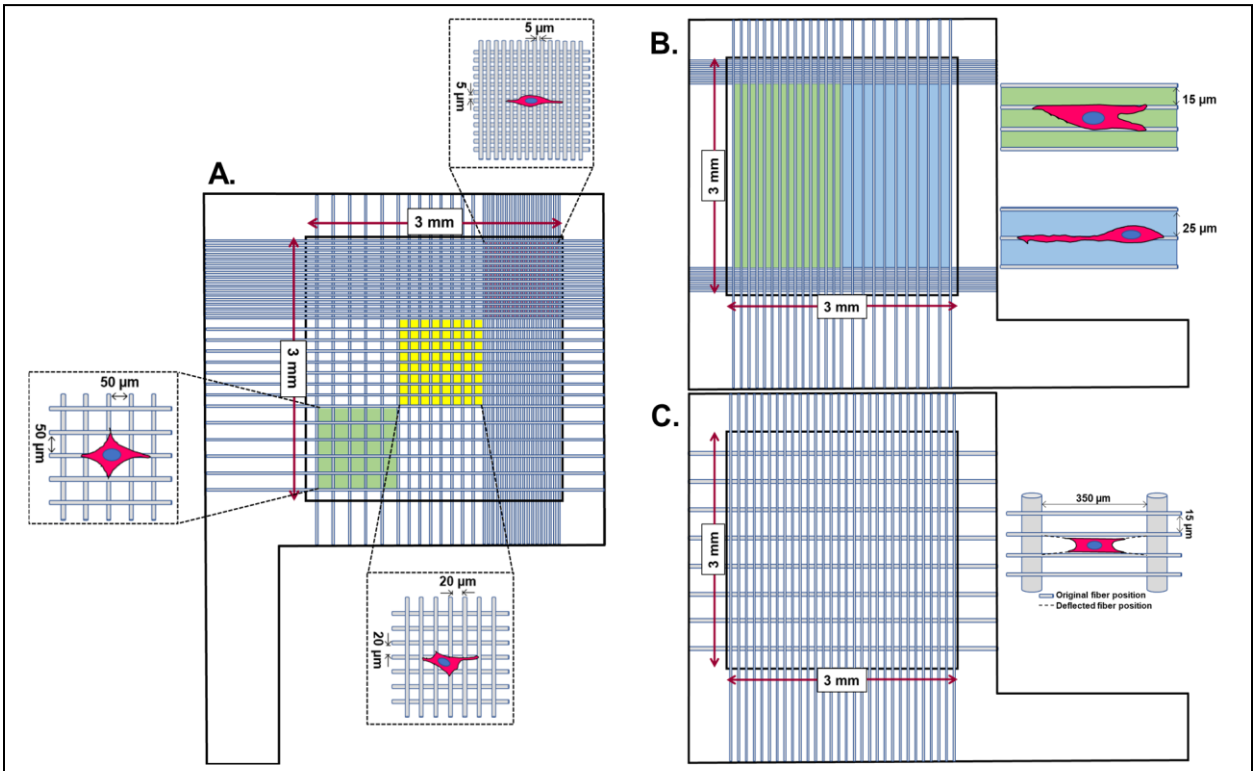

Figure 2.2. Three scaffold types were fabricated to monitor various parameters of cell dynamics. a) Crosshatch fibrous scaffolds of three mesh sizes were used to modulate cell morphology. b) Parallel fibrous scaffolds were used to observe migration dynamics. c) Force scaffolds were used to quantify cell contractile force exertion.

Fiber Fusing. After spinning, the scaffolds were treated with the vapor phase of tetrahydrofuran (THF), a good solvent for polystyrene, resulting in each fiber intersection being fused together. To this end, a glass Petri dish was filled ¾ of the way with THF and placed in the bottom center of a desiccator. Scaffolds were attached by the stub to the edge of a copper tape coated scanning

electron microscopy (SEM) stand. The SEM stand was placed in the middle of the desiccator grate atop a circular piece of aluminum foil to protect the fibers from being overexposed, and consequently over fused from the direct exposure to the THF vapor (Figure 2.3).

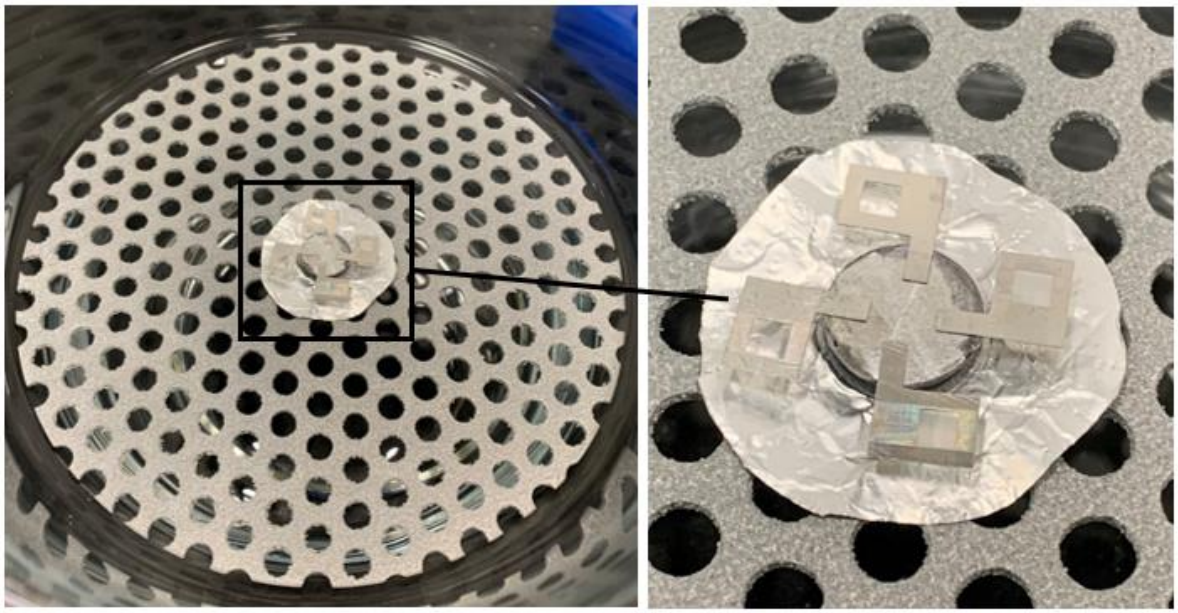

Figure 2.3. Fiber fusing was performed to ensure the integrity of the fiber networks. Scaffolds were mounted on an SEM stand and placed in a desiccator filled with THF fumes to fuse the fibers.

Subsequently, the gasket and lid of the desiccator were replaced, and the scaffolds were allowed to sit in the desiccator for 20 minutes at atmospheric pressure. During this time, THF evaporated and filled the space of the desiccator, slightly deforming the fibers. The fusing time was sufficient to create fixed fiber-fiber and fiber-scaffold intersections and short enough to maintain proper inter-fiber spacing. Figure 2.4 shows representative SEM images of the fused intersections between fibers.

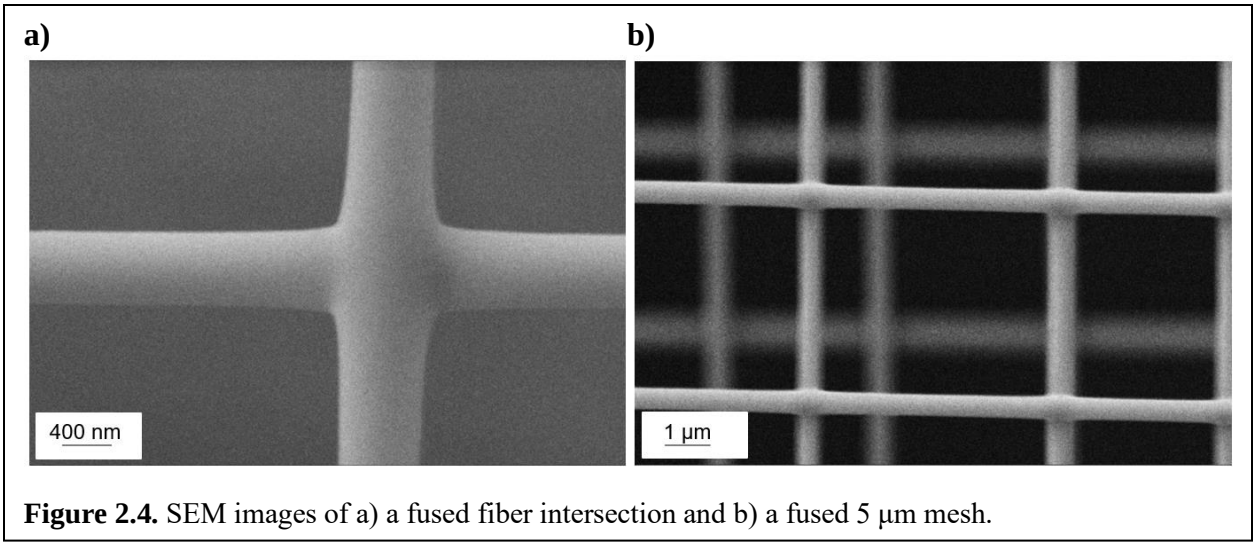

Figure 2.4. SEM images of a) a fused fiber intersection and b) a fused 5 µm mesh.

2.2 Host cell-pathogen Interaction Assay Preparation

Preparing Scaffold for Cell Seeding. A 40 mm partial glass bottom petri dish was soaked in a 1:16 barbicide to water solution for 30 minutes, rinsed with DI water, sprayed with 70% ethanol, and left under UV light for thirty minutes. The stub of the fiber-coated scaffold was attached to the glass well of the petri dish using a small amount of vacuum grease. 70% ethanol was added in the sides of the well to completely submerge the scaffold without destroying the fiber networks. After 10 minutes, ethanol was carefully removed, and the petri dish was washed twice with PBS to remove any remnants of ethanol. Lastly, fibronectin from bovine plasma (4 µg/mL) was introduced and allowed to submerge the scaffold for one hour before removing and introducing fibroblasts to facilitate cellular attachment and recapitulate the proteinaceous extracellular environment.

Mammalian Cell Culture. NIH/3T3 mouse embryo fibroblasts (ATCC CRL-1658) were cultured at 37˚C and 5% CO_2 in tissue culture treated T-25 flasks containing high glucose Dulbecco's Eagle Medium (DMEM) supplemented with 10% Fetal Calf Serum (FCS). Before seeding, fibroblasts were washed twice with PBS, introduced to 0.75 mL of .25% (w/v) trypsin for five minutes,

centrifuged at 1000 RCF for 1.5 minutes, and resuspended in 2-3 mL of media. Subsequently, 35 μL of fibroblasts were seeded on the scaffold at a density of 20×10^4 cells/mL and allowed to attach to the fibers for an hour before flooding the petri dish with 2 mL of cell media.

Bacteria Culture. *Pseudomonas aeruginosa* PA14 mKO and PAO1 (both strains were gift from George O'Toole, Dartmouth University) colonies were grown on 0.5% NaCl Lysogeny Broth (LB) agar plates at 37˚C for 12 hours. One colony was chosen and cultured in a 15 mL test tube containing 5 mL of 0.5% NaCl LB (pH 7.0) at 37˚C and 150 RPM for 13 hours. 1 mL of bacteria suspension was taken from the overnight culture and centrifuged for 8 min at 3000 RCF and resuspended in 1 mL high glucose DMEM supplemented with 10% FCS. Finally, bacteria were introduced at a multiplicity of infection (MOI) of 22:1 (22 bacterium to every 1 fibroblast) to the petri dish containing the fibroblast populated scaffold.

2.3 Cell Imaging

Optical Imaging. A Zeiss AxioObserver Z1 inverted microscope equipped with an AxioCam MRm camera and 20× objective was used to capture each experiment (Zeiss Microscopy, Oberkochen, Germany). Before bacteria introduction, cells were imaged every minute for a minimum of three hours and a maximum of four hours. Post-PA14 mKO introduction, imaging was performed using the experimental designer function which alternated between 14 minutes of brightfield imaging and one minute of both mOrange fluorescent and brightfield imaging, until all cells were dead. Post-PAO1 introduction, imaging was performed every minute only using the brightfield filter until all cells were dead.

Scanning Electron Microscopy. Field Emission Scanning Electron Microscopy (FESEM) was used to capture images of the suspended fibers and corroborate target values for fiber diameter and

spacing between fibers. Prior to imaging, scaffolds were placed in the middle of copper tape covered SEM stands and coated with a 5.5 nm thick layer of platinum-palladium using a Leica sputter coater (Leica, Wetzlar, Germany). Images were captured with an electron beam voltage of 5 kV at a working distance of 8 mm. Magnifications of 60 k and 20 k were used to best capture fiber diameters and inter-fiber spacing, respectively. ImageJ was used to process SEM images to obtain fiber diameter and spacing values.

Immunofluorescence Imaging. Fixed immunofluorescence staining was performed on the fibroblasts with and without exposure to bacteria to visualize changes in f-actin and the nucleus. Cells were fixed with 4% paraformaldehyde for 15 minutes, washed twice with PBS, and subsequently permeabilized with 0.1% Triton X-100 in PBS solution for 15 minutes. After washing twice more with PBS, rhodamine-conjugated phalloidin and Hoechst 33342 were diluted in an antibody dilution buffer in 1:80 and 1:30 ratios, respectively, and 300 μL of the solution containing the aforementioned dye concentrations was added to each petri-dish well. Samples were stored in a dark drawer for 45 minutes followed by 3 PBS washes. Immunofluorescence imaging was performed using a confocal microscope (LSM 880; Carl Zeiss) and a 63×, 1.15 NA water-immersion objective.

2.4 Quantitative Analysis Methods

Spread Area and Circularity Analysis. Time lapse videos captured temporal changes in cell morphology during bacterial invasion. Cell area and circularity were analyzed every ten minutes until drastic observable changes in circularity occurred, at which parameters were obtained every 1-5 minutes until cell death. The final timepoint in cell death was taken to be the timepoint wherein cell membrane was disrupted, as observed in phase contrast microscopy. Figure 2.5 shows

representative phase-contrast microscopy images of a fibroblast before and after cell death. Before death (Figure 2.5a), the fibroblast had a circular and well-defined membrane. However, within one minute, the cell membrane was no longer defined and was evidently disrupted (Figure 2.5b).

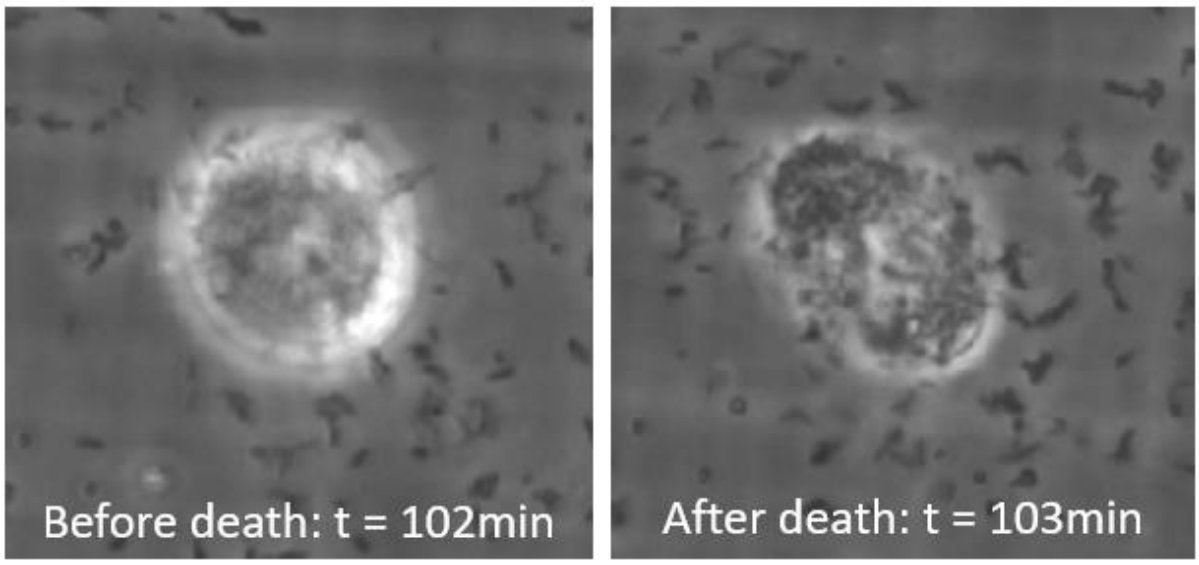

Figure 2.5. Representative phase-contrast microscopy of a fibroblast a) before death with largely intact membrane and b) after death with disrupted membrane.

The freehand selections function in ImageJ was used to outline each cell and output several parameters, including area and perimeter. Circularity (∅) was evaluated using the following equation:

$$\emptyset = \frac{4\pi A}{P^2},$$

where A represents cell spread area and P represents cell perimeter. Two circularity related parameters were used to categorize individual cell deaths as sharp (sudden) or gradual. The rate of change of circularity was calculated between adjacent time points over the course of cell death. To be considered a sharp shape change to death, the rate of change of circularity must be greater than or equal to, either 0.04 over a time period of ten minutes, or 0.1 over a time period between one

minute and ten minutes. In addition, the maximum cell circularity must meet or exceed a value of 0.7. Cell deaths which did not meet these criteria were considered gradual.

Migration Analysis. The freehand selections function in ImageJ was also used to track the x and y positions of the cell centroid at each time point. Using these coordinates, several migration parameters were calculated over the course of invasion. Instantaneous speed (s) was calculated using the distance formula over adjacent time points:

$$s = \frac{distance}{time} = \frac{\sqrt{(x_2 - x_1)^2 + (y_2 - y_1)^2}}{(t_2 - t_1)}.$$

Cell persistence (P) was calculated by dividing the displacement by the total path length traveled, as shown in the following equation:

$$P = \frac{displacement}{total\ path\ length} = \frac{\boldsymbol{r}_{final} - \boldsymbol{r}_{inital}}{\sum_{i=0}^{i=final} |\boldsymbol{r}_i - \boldsymbol{r}_{i-1}|},$$

where displacement is a vector, whose length is the shortest distance from the initial to final position, and the total path length is the sum of all distances travelled between the initial and final positions. Accordingly, a persistence of one indicates the cell has travelled in a straight line away from its initial position since the displacement is exactly equal to the total path length.

Force Analysis. Due to fused fiber intersections, force fibers (200 nm in diameter) were modeled as beams with fixed-fixed boundary conditions to the base fibers (2 μm in diameter). Finite Element Method (FEM) was used to discretize the force fibers into a finite number of uniform straight beam elements. The following fourth order differential equation was used to model the transverse deflection of the beam:

$$\frac{d^2}{dx^2}\left(EI\frac{d^2v}{dx^2}\right) - \frac{d}{dx}\left(P\frac{dv}{dx}\right) = f(x)\,; \qquad 0 < x < L$$

where E is modulus of elasticity, I is the beam moment of inertia, P is the actual value of the tensile load at a cross-section along x-axis, and v is the transverse deflection of the beam along y-axis (Sheets et al. 2016). In addition, this equation assumed the length of the beam to lie along the x -axis and transverse to the y-axis and that $f(x)$ be a transversely distributed load along y-axis.

An optimization framework was also used to back calculate the cell contractile force exerted on horizontal force fibers from the resulting fiber deflection positions. To achieve this, A built-in MATLAB Gradient Based Optimizer (GBO) was utilized. In the cell model, it was assumed that all forces were acting along the dominant stress fiber located at the focal adhesion cluster at each end of the cell body. The goal of optimization was to minimize $g(x)$ which is defined by the following equation:

$$g(x) = \frac{1}{2}\left|\left|V_{EXP} - V_{FEM}\right|\right|^2$$

Where, V_{EXP} is the vector of vertical displacements (v_i) generated after interpolating the experimental vertical displacements and V_{FEM} is the vector of computational vertical displacements from finite element model.

The time lapse video of interest was loaded from ImageJ into MATLAB and six points of interest were selected: two points on each fiber span equidistant from the cell extremities and base fibers, two points on each cell extremity, and two points on the cell body equidistant from the cell extremities. The points selected on the fiber span and cell body were used to fit the best equation to the deflected fiber whereas both points on the cell extremities were used to calculate forces exerted by the cell. Force and deflection measurements were obtained every 10-20 minutes until drastic observable changes occurred during the death phase, at which analysis was performed every 1-5 minutes. Frequency of analysis was dependent on observable changes in cell morphology.

Statistical Analysis. Minimally, duplicate independent experiments were run for each assay. Statistical analysis was performed using JMP Pro 15 (SAS Institute Inc, Cary, NC, USA) software. Tukey's honestly significant difference (HSD) test was used to test the statistical significance between more than two groups and Student's t tests were utilized for comparisons between only two groups. Data fits were performed in either MATLAB or Microsoft Excel. For MATLAB boxplots, the central mark indicates the median while the bottom and top edges of the box indicate the 25th and 75th percentiles, respectively. Whiskers extend to nonoutlier maximums. Outliers are considered to be values that are more than 1.5 interquartile ranges (IQR)s away from the top or bottom of the box and are noted using the '+' symbol. Standard values for reporting significance were used.

Chapter 3. Characterization of Fibroblasts During *P. aeruginosa* Invasion

In this chapter we report our findings on the role of cell shape on NIH/3T3 fibroblasts invasion by *P. aeruginosa*. *P. aeruginosa* strains PAO1 and PA14 were chosen as the representative invasive and cytotoxic strains, respectively. Moreover, we investigated how fibroblast contractile force exertion is regulated during interaction with *P. aeruginosa*. Our results suggest that fibroblast morphology and strain of *P. aeruginosa* introduced both play a role in modulating host-cell morphodynamics and contractility over the course of invasion. We were also able to correlate these changes with differing actin stress fiber configurations.

3.1 Cytotoxic and Invasive *P. aeruginosa* Strains Induce Significantly Different Death Times

Firstly, it was sought to ascertain if fibroblast morphology and differing configurations of the cell cytoskeleton had any effect on time of cell death. Five different cell morphologies were produced using the various polystyrene fiber architectures described in Figure 2.2a,b. Flat 2D polystyrene was used as the baseline control. Time of death was taken to be from the time of bacteria introduction ($t = 0$) to the time of cell death at which the cell membrane was evidently disrupted (Figure 2.5b), often antecedent by blebbing. Fibroblast cells in each of these six different morphologies were exposed to the cytotoxic *P. aeruginosa* PA14 first. No significant differences in time of death were found between any of the cell morphologies for cells exposed to PA14 (Figure 3.1a). We next investigated the effect of cell morphology on time of cell death for fibroblast interacting with the invasive *P. aeruginosa* PAO1. Overall, time to cell death increased significantly, compared to that of cells interacting with the PA14 strain for all cell morphologies ($p < 0.0001$). Due to the observably longer death times of cells exposed to PAO1, it was speculated that a difference in death time may emerge for cells of varied morphologies. Surprisingly, it was

also found that although PAO1 took longer to induce cell death, there was no significant difference in death time between any of the cell morphologies (Figure 3.1a). Unsurprisingly, when combining death times for all morphologies treated with each of the two strains, it was found that the time of death between PAO1 and PA14 exposed cells was significantly different ($p < 0.0001$) (Figure 3.1b). In fact, the average time of death for cells exposed to PAO1 (264 ± 75 min) was almost 2.5× that of cells exposed to PA14 (107 ± 27 min). This may be attributed to the cytotoxic factors PA14 is capable of releasing into the environment coupled with the requirement of PAO1 to interact with the cell surface in order to induce cell death, resulting in a large disparity in death time between the two strains.

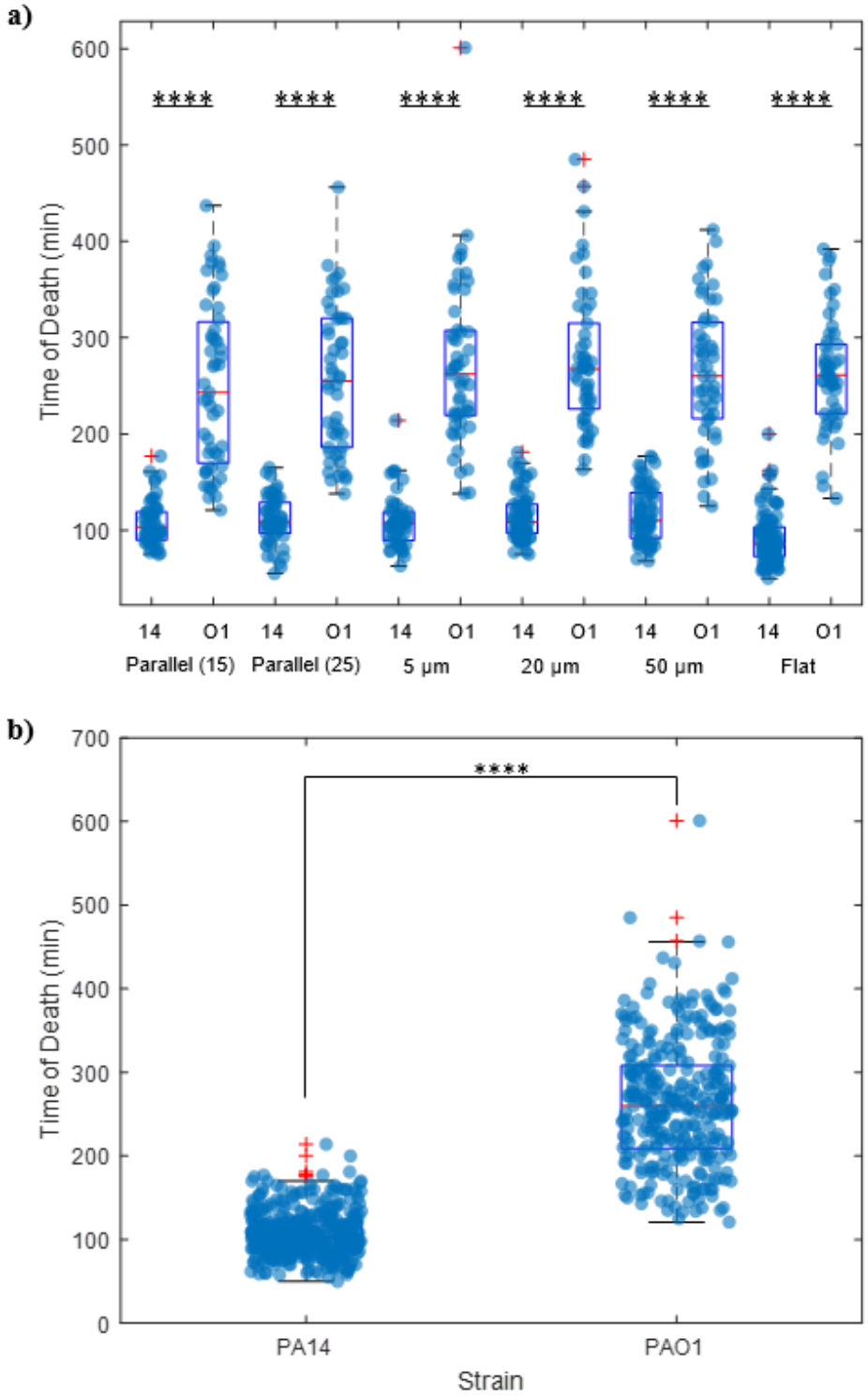

Figure 3.1. a) The time of cell death was compared across the following fibroblast cell morphologies treated with cytotoxic PA14 or invasive PAO1, respectively: parallel (15) (N = 54, 51), parallel (25) (N = 54, 50), 5 µm (N = 53, 51), 20 µm (N = 72, 50), 50 µm (N = 69, 50), and flat (N = 94, 50). No significant differences were found between morphologies treated with the same bacteria strain. b) Time of cell deaths were accumulated for cells treated with each bacteria strain. ****p-value < 0.0001.

3.2 Fiber Configurations Module Cell Spread Area

Given our goal of investigating the role of cell morphology on its interaction with *P. aeruginosa*, we first investigated how fiber network spacing and architecture (single parallel layer vs crosshatch double layer) modulate fibroblast cell spread area. Cells on the crosshatched fibers with 20 μm or 50 μm mesh sizes as well as on the flat 2D surface took on spread morphologies (Fig 3.2a-c), whereas cells on the 5 μm spaced crosshatch and single layer of parallel fibers with 15 μm or 25 μm spacing had similarly elongated morphologies (Figure 3.2a, e, and f). Within the three aforementioned spread morphologies, cells on the 50 μm mesh tended to exhibit kite-like shapes with high aspect ratios, whereas cells on the 20 μm mesh and flat surface had defined leading and trail edges. Qualitative results were consistent with a previous study from the Nain Lab which explored differences in Hras1 thyroid cancer cell morphologies on a flat 2D surface and crosshatched meshes (Jana et al. 2019).

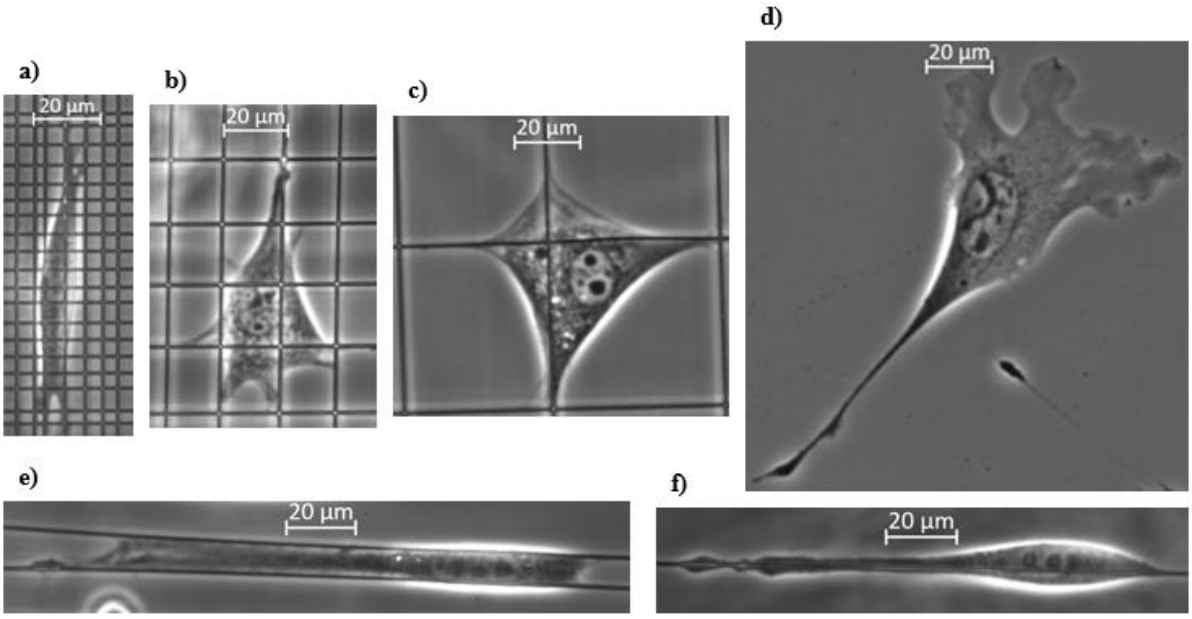

Figure 3.2. Representative images of nanofiber networks and the corresponding cell morphologies on (a) crosshatch 5 μm mesh, (b) crosshatch 20 μm mesh, (c) crosshatch 50 μm mesh (d) flat 2D, (e) parallel large spacing fibers, and (f) parallel small spacing fibers. All fiber networks were constructed using 550 nm diameter suspended polystyrene fibers.

Subsequently, initial spread area data was gathered for each cell morphology prior to bacteria introduction. The initial spread area for an individual cell was obtained by averaging the two area values from t = 0 and t = 10 minutes. These values were compared across six morphologies, as shown in Figure 3.3.

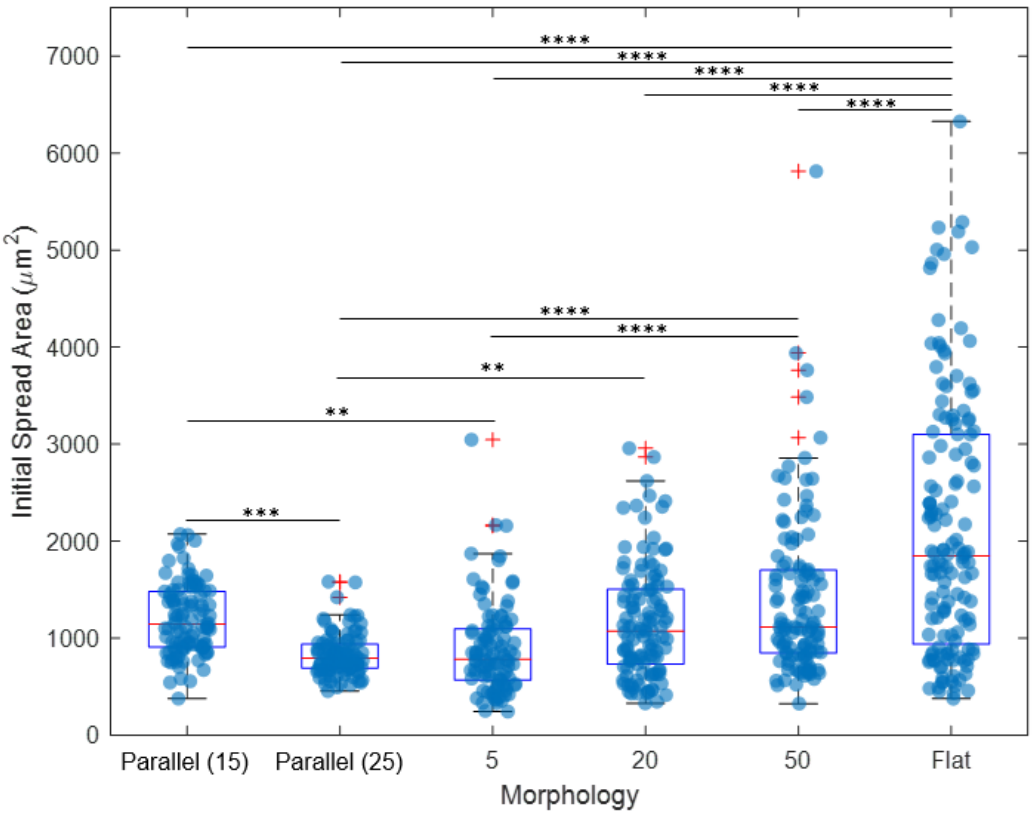

Figure 3.3. Initial spread area data was compared across the following cell morphologies: parallel (15) (N = 105), parallel (25) (N = 104), 5 µm (N = 104 20 µm (N = 122), 50 µm (N = 119), and flat (N = 144). **p-value < 0.01, ***p-value < 0.001, ****p-value < 0.0001.

Cells on the 2D flat surface had the largest spread area (2113 ± 1318 μm^2) while cells on the dense crosshatch network (5 µm mesh size) had the smallest spread area (884 ± 462 μm^2) of the cells on crosshatched meshes, consistent with results from the previously mentioned study that used Hras1 thyroid cancer cells (Jana et al. 2019). As expected, the two networks that produced spindle-like elongated morphologies, 5 µm meshes and parallel fibers with large spacing, did not give rise to significant difference. However, the parallel fibers with small spacing, which also produced

elongated cells, gave rise to significant differences with the 5 μm mesh ($p < 0.0001$) and parallel fibers with large spacing ($p < 0.0001$). This is due to small spacing parallel cells being characterized by elongated rectangular morphologies as opposed to spindle-like morphologies. Rather, parallel cells showed similar spread area values to cells on the intermediate spaced mesh (20 μm).

3.3 Fiber Configurations and *P. aeruginosa* Strain Type Modulate Cell Circularity and Mode of Death

Next, change in fibroblast morphology was quantified using the circularity parameter. Circularity data was used to elucidate more information about the cell shape as opposed to just the cell size information obtained using the cell spread area data. Similar to the spread area analysis, initial circularity data was gathered for all six morphologies before bacteria introduction, again by averaging the values at t = 0 and t = 10 minutes for each cell (Figure 3.4). Unsurprisingly, both the large (0.07 ± 0.04) and small spacing (0.07 ± 0.04) parallel cells, which had the most elongated morphologies, had significantly lower initial circularity values than all other categories. Contrastingly, cells on the 5 μm spaced mesh had the greatest average initial circularity (0.22 ± 0.13) attributed to small perimeter values which greatly affect the circularity parameter.

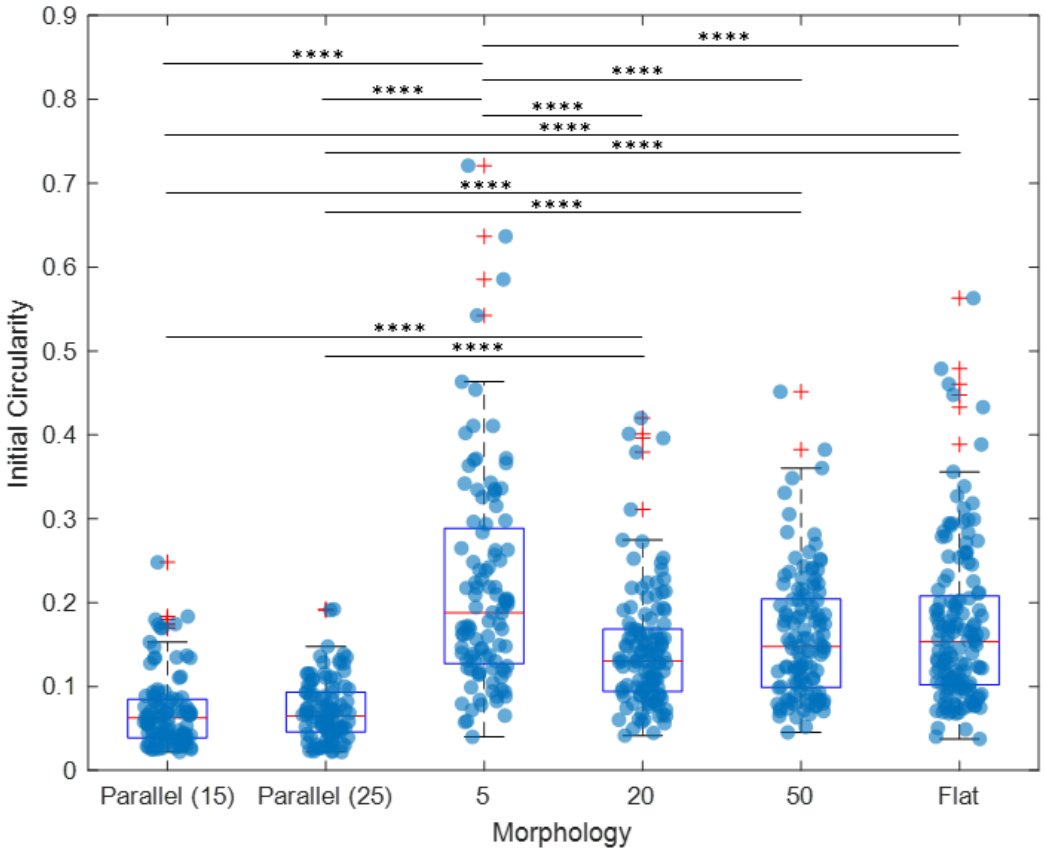

Figure 3.4. Initial circularity data was compared across the following cell morphologies: parallel (15) (N = 105), parallel (25) (N = 104), 5 µm (N = 104 20 µm (N = 122), 50 µm (N = 119), and flat (N = 144). ****p-value < 0.0001.

Next, we studied temporal changes in cell circularity over time. Time-lapse images of cells interacting with bacteria suggested two distinct modes of cell shape change to cell death: sharp and gradual. Representative image sequences of cells on a 50 µm spaced mesh dying by sharp and gradual deaths can be seen in Figure 3.5. In the sharp mode of death, cells transformed from elongated, spread-out morphologies into circular, balled-up morphologies. In experimental videos, this mode of death is qualitatively evident as cells quickly pull in their protrusions in an elastic manner (Fig. 3.5a). The cell dying by sharp death elastically balled up within a span of approximately three minutes and subsequently pulled in its protrusions (Figure 3.5a). This dynamic is thought to be a result of loss of contractility due to bacterial interference with

cytoskeletal components, such as actin, responsible for maintaining the shape of the cell. By contrast, cells exhibiting gradual deaths had either little morphological transformation, dying with their protrusions extended in the same positions as they started, or gradually balled-up over the entire course of invasion, seemingly able to maintain some contractility (Fig. 3.5b).

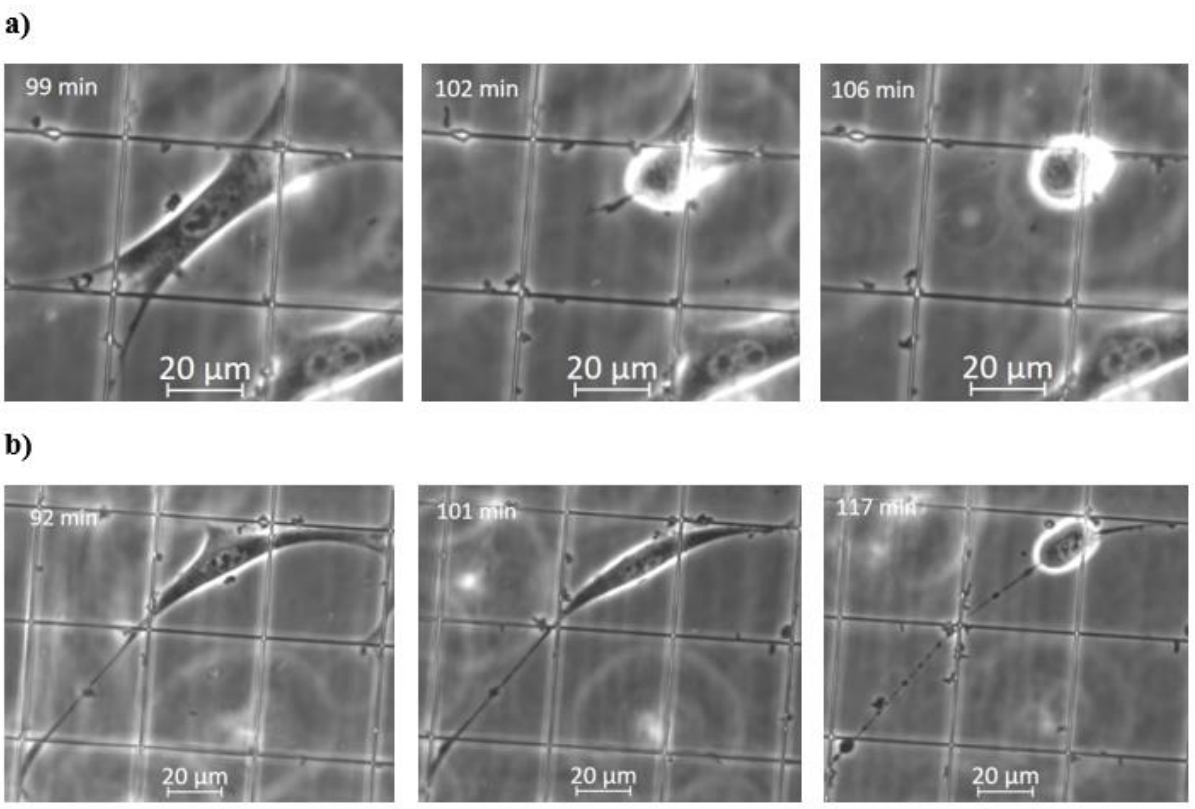

Figure 3.5. Representative image sequences of a cell dying on a 50 µm crosshatch network by a) sharp death b) and gradual death. The cell dying by sharp death elastically transforms and pulls in its protrusions while the latter remains in its initial position.

All of the factors which dictate the manner of death is not known; however, the death type was found to be highly dependent on cell morphology as a result of scaffold type (Table 3.1). During PA14 invasion, fibroblasts on the 20 µm spaced mesh were most likely to die by means of a sharp death with 72.2% deaths categorized as sharp. Similarly, 68.1% of the cells on flat and 5 µm mesh experienced sharp death. There was an almost even split in death type for cells on 50 µm mesh and parallel fiber with large spacing. By contrast, fibroblasts on parallel fibers with small spacing only

died by manner of sharp death 38.9% of the time. The small spacing parallel morphology was the only morphology in which percent gradual was greater than percent sharp. The manner of death was also found to be dependent on which *P. aeruginosa* strain was introduced to the fibroblasts (Table 3.1). In contrast to PA14 results, cells exposed to PAO1 were more likely to die by gradual death for all morphologies. A strong majority of cells (≥84%) experienced gradual death with the cells on the 20 μm spaced mesh exclusively undergoing gradual death. Due to the large difference in occurrence of sharp deaths between PA14 and PAO1 exposed cells, we expect that the differential expression of various virulence factors discussed previously for cytotoxic and invasive strains, such as the increased ability of PA14 to regulate density dependent gene expression through quorum sensing, may be related to the manner of death.

Table 3.1. Death Type for each Fibroblast Cell Morphology and Bacteria Strain.

		Flat	50	20	5	Parallel (25)	Parallel (15)
PA14	Count	94	69	72	53	54	54
	%Sharp	68.1	56.5	72.2	67.9	55.6	38.9
	%Gradual	31.9	43.5	27.8	32.1	44.4	61.1
PAO1	Count	50	50	50	51	50	51
	%Sharp	4.0	20.0	0	11.8	16.0	7.8
	%Gradual	96.0	80.0	100	88.2	84.0	92.2

Temporal changes in cell circularity for all the cases summarized in Table 3.1 are shown in Figures 3.6-3.11, where sharp and gradual modes of death are displayed for each morphology and bacteria strain combination. By visualizing changes in circularity over time, similarities can be found between morphologies that otherwise are not connected. For example, flat (Figure 3.6) and large spacing parallel (Figure 3.10) cells exposed to PA14 seem to have similar circularity trends; many gradual cells did not meet the time rate of change of circularity requirement but met the minimum circularity requirement of 0.7 after a drawn-out period. By contrast, it can be seen in Figures 3.8b

and 3.9b for 5 μm and 20 μm morphologies, respectively, none of the gradual cells exposed to PA14 satisfied either of the sharp death criteria.

For cells exposed to PAO1, it can be seen that many cells did eventually reach the minimum circularity requirement to be categorized as sharp, but most did not reach the rate of change of circularity requirement. In fact, of all the cell morphologies exposed to PAO1, cells on the 5 μm mesh were most likely to meet the minimum circularity requirement with 50% of cells reaching a circularity of 0.7 or above. However, less than 12% of these cells also met the rate of change of circularity requirement to be considered a sharp death.

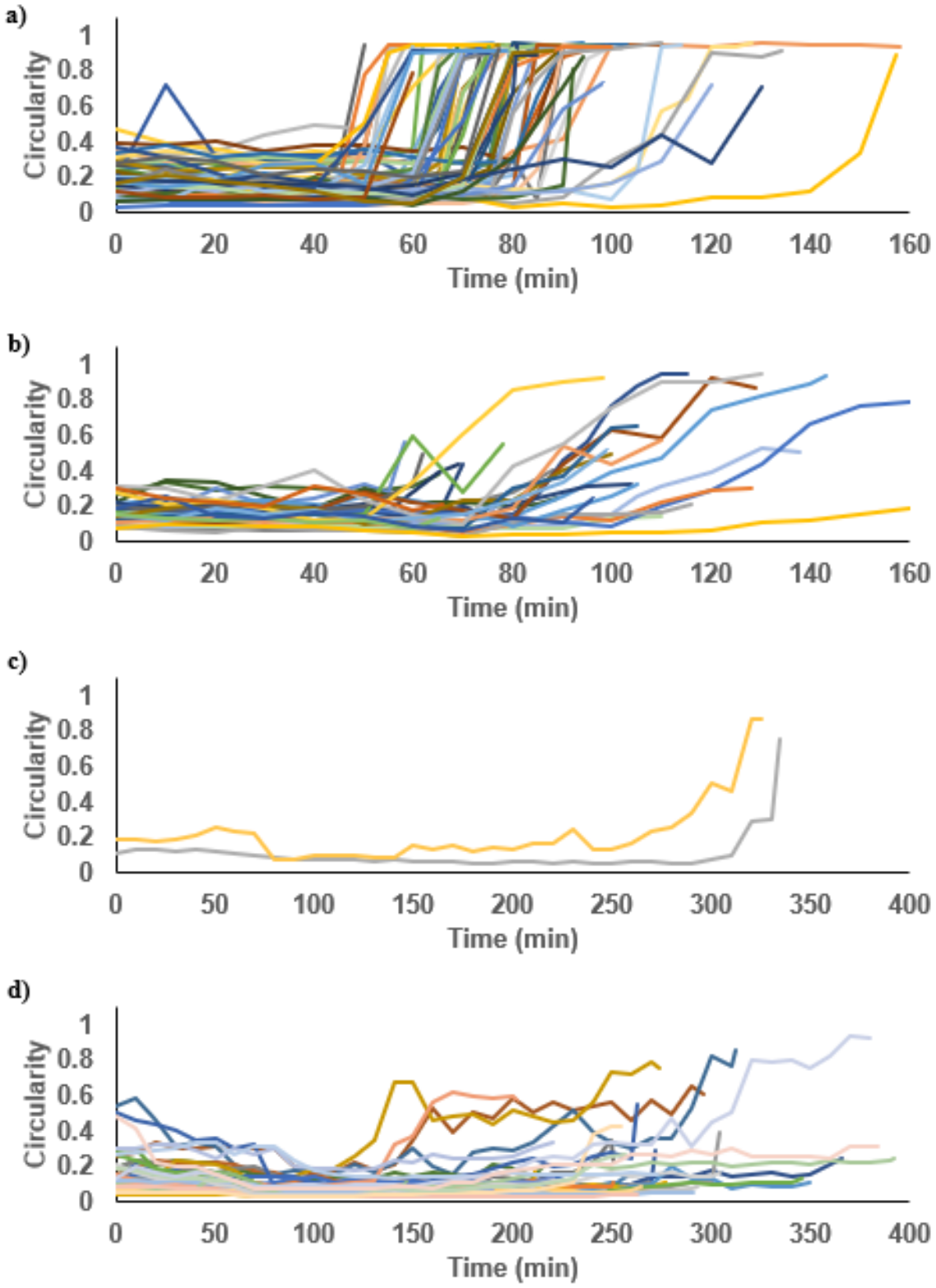

Figure 3.6. Sharp and gradual modes of death were isolated for cells on the 2D flat surface to identify further trends: a) PA14 sharp (N = 64), b) PA14 gradual (N = 30), c) PAO1 sharp (N = 2), d) PAO1 gradual (N = 48).

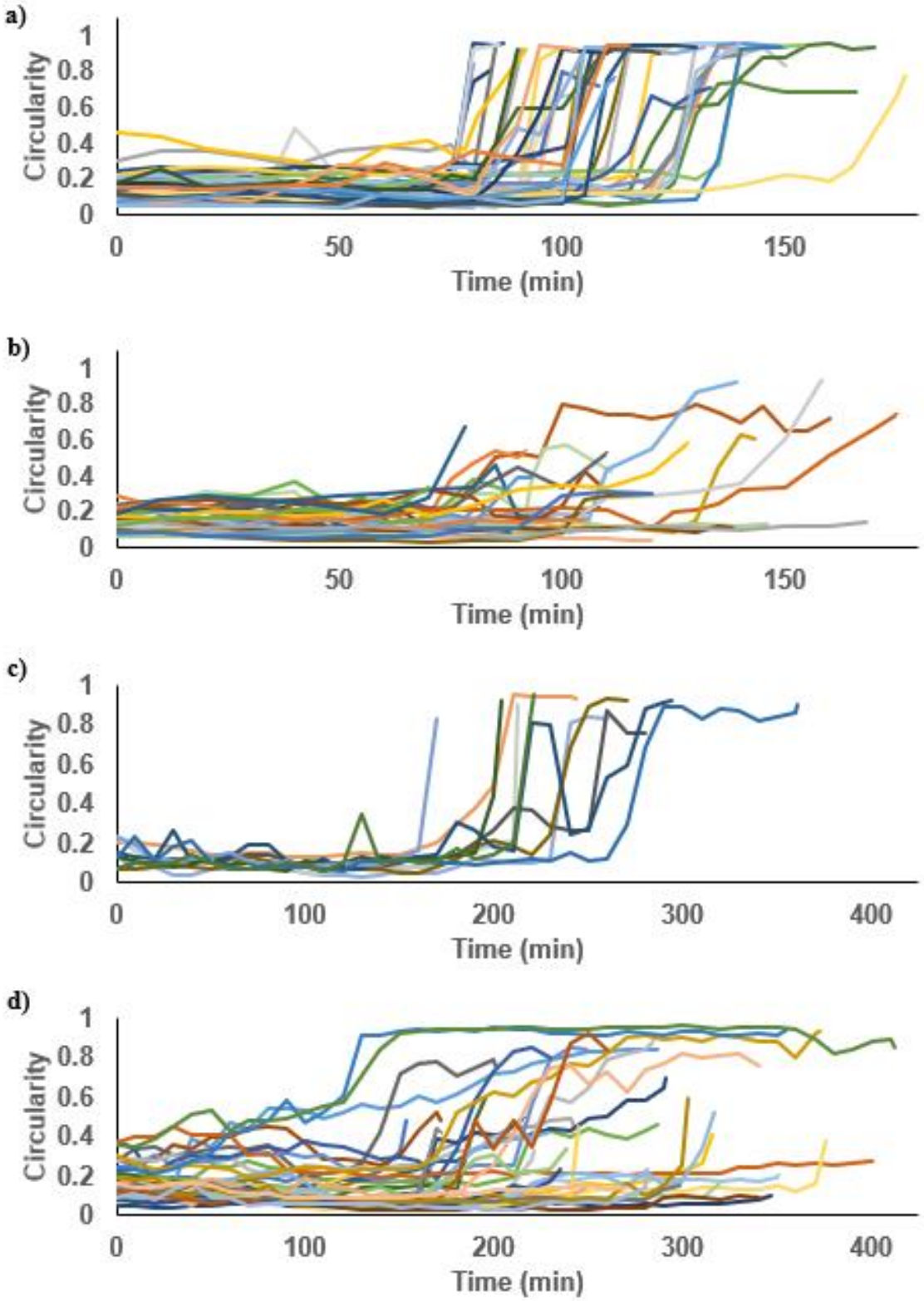

Figure 3.7. Sharp and gradual modes of death were isolated for cells on the 50 μm mesh network to identify further trends: a) PA14 sharp (N = 39), b) PA14 gradual (N = 30), c) PAO1 sharp (N = 10), d) PAO1 gradual (N = 40).

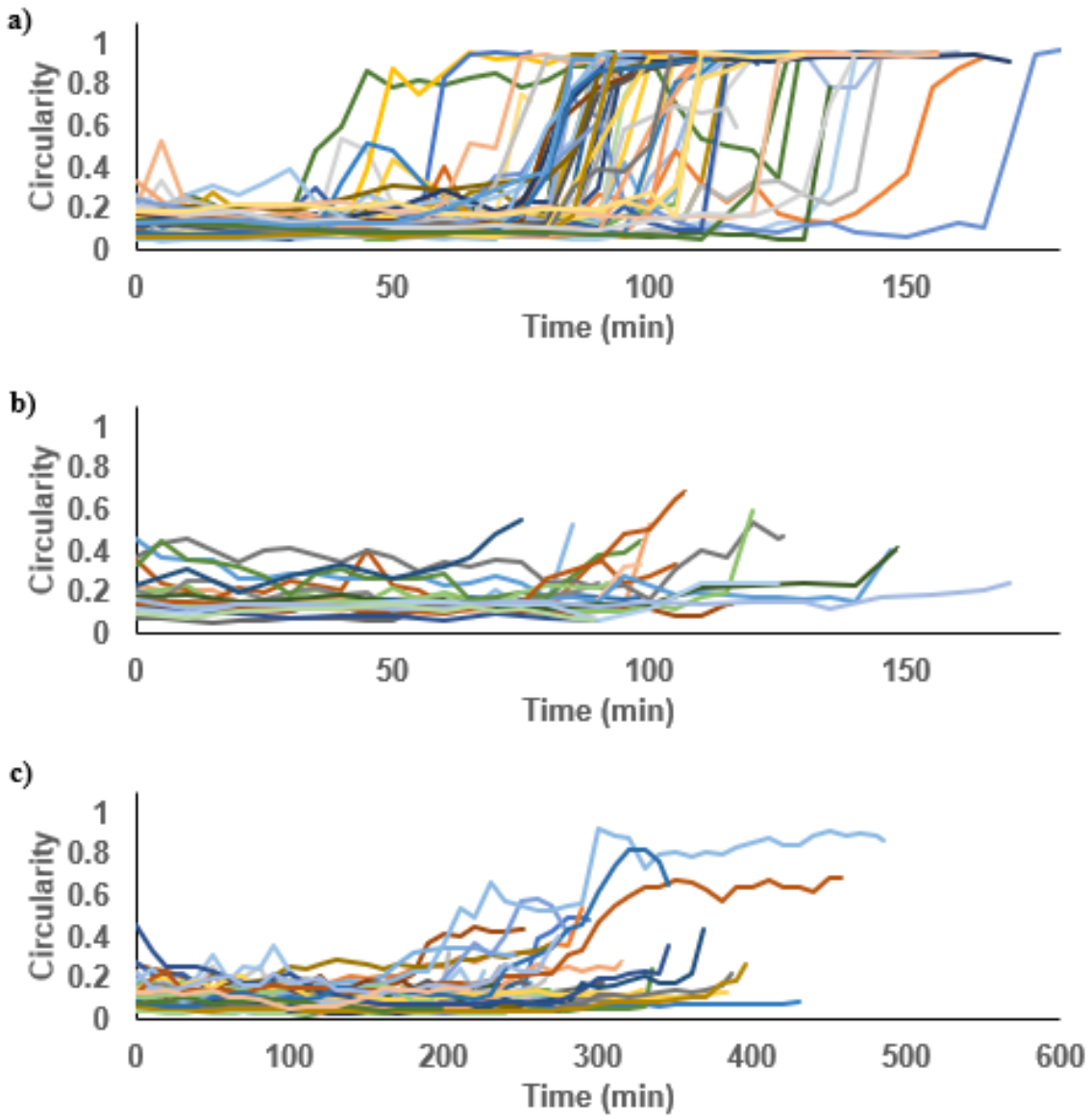

Figure 3.8. Sharp and gradual modes of death were isolated for cells on the 20 μm mesh network to identify further trends: a) PA14 sharp (N = 52), b) PA14 gradual (N = 20), c) PAO1 gradual (N = 50). No sharp death was observed in cells interacting with PAO1.

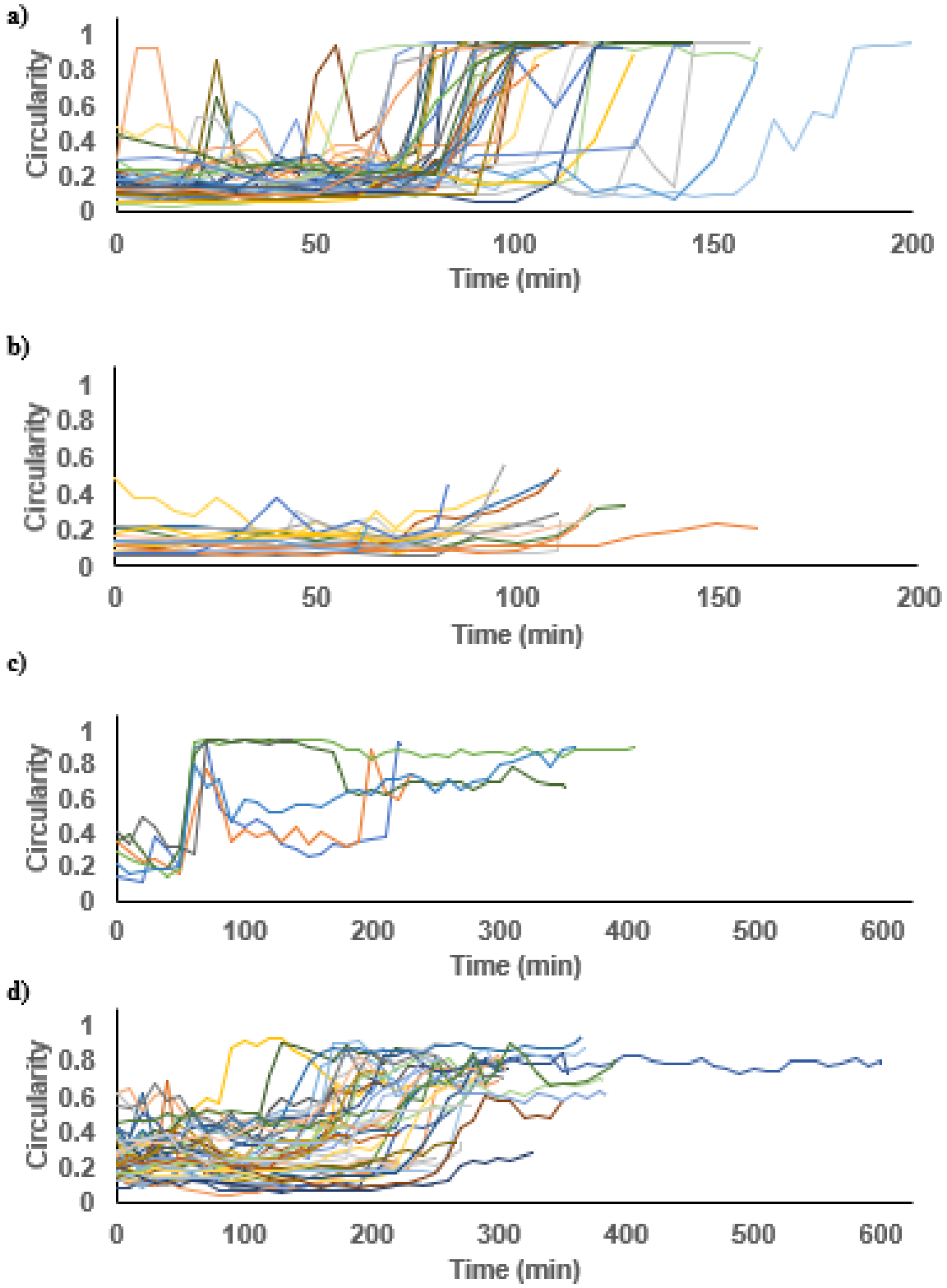

Figure 3.9. Sharp and gradual modes of death were isolated for cells on the 5 μm mesh network to identify further trends: a) PA14 sharp (N = 36), b) PA14 gradual (N = 17), c) PAO1 sharp (N = 6), d) PAO1 gradual (N = 45).

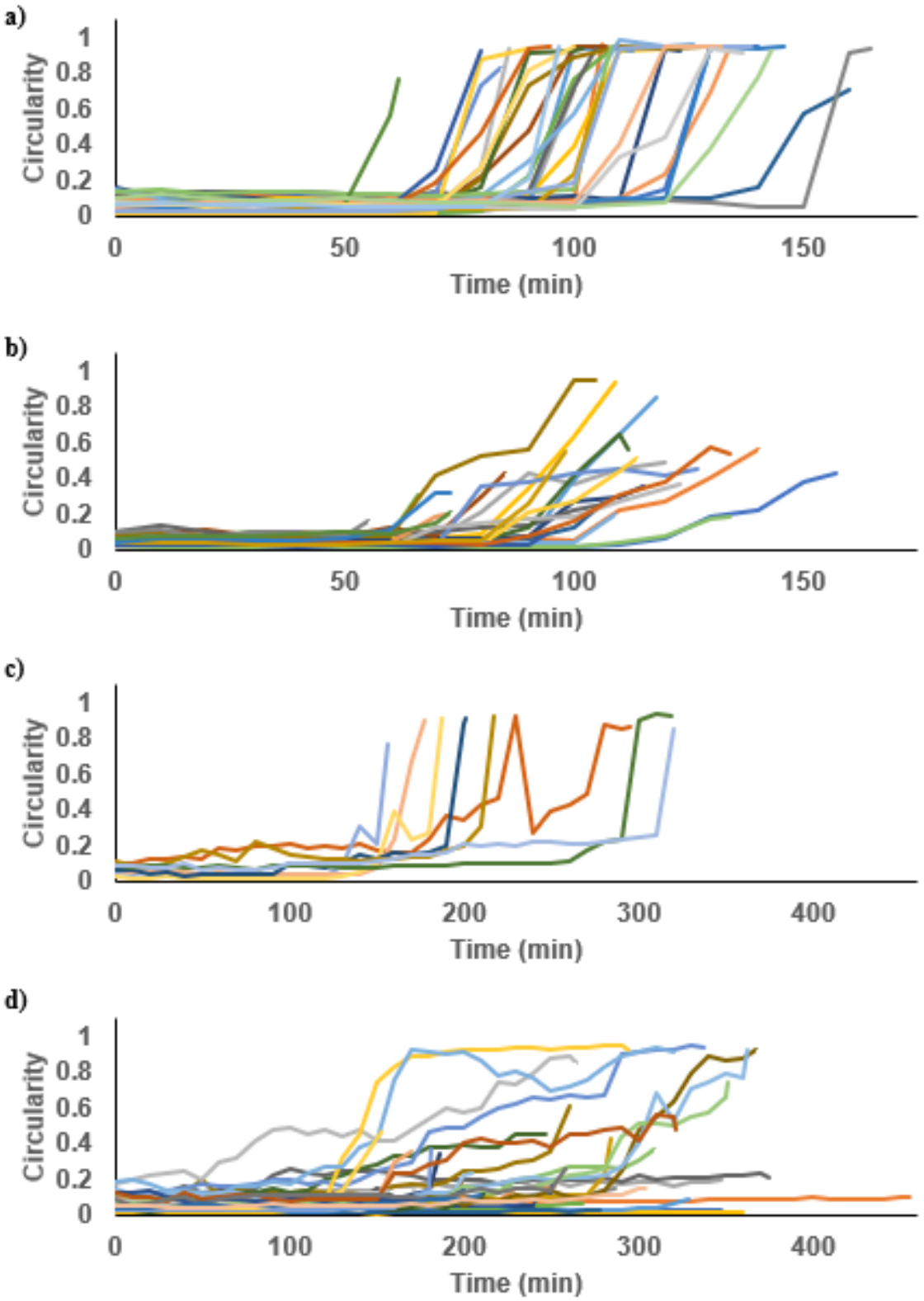

Figure 3.10. Sharp and gradual modes of death were isolated for large spacing parallel cells to identify further trends: a) PA14 sharp (N = 30), b) PA14 gradual (N = 24), c) PAO1 sharp (N = 8), d) PAO1 gradual (N = 42).

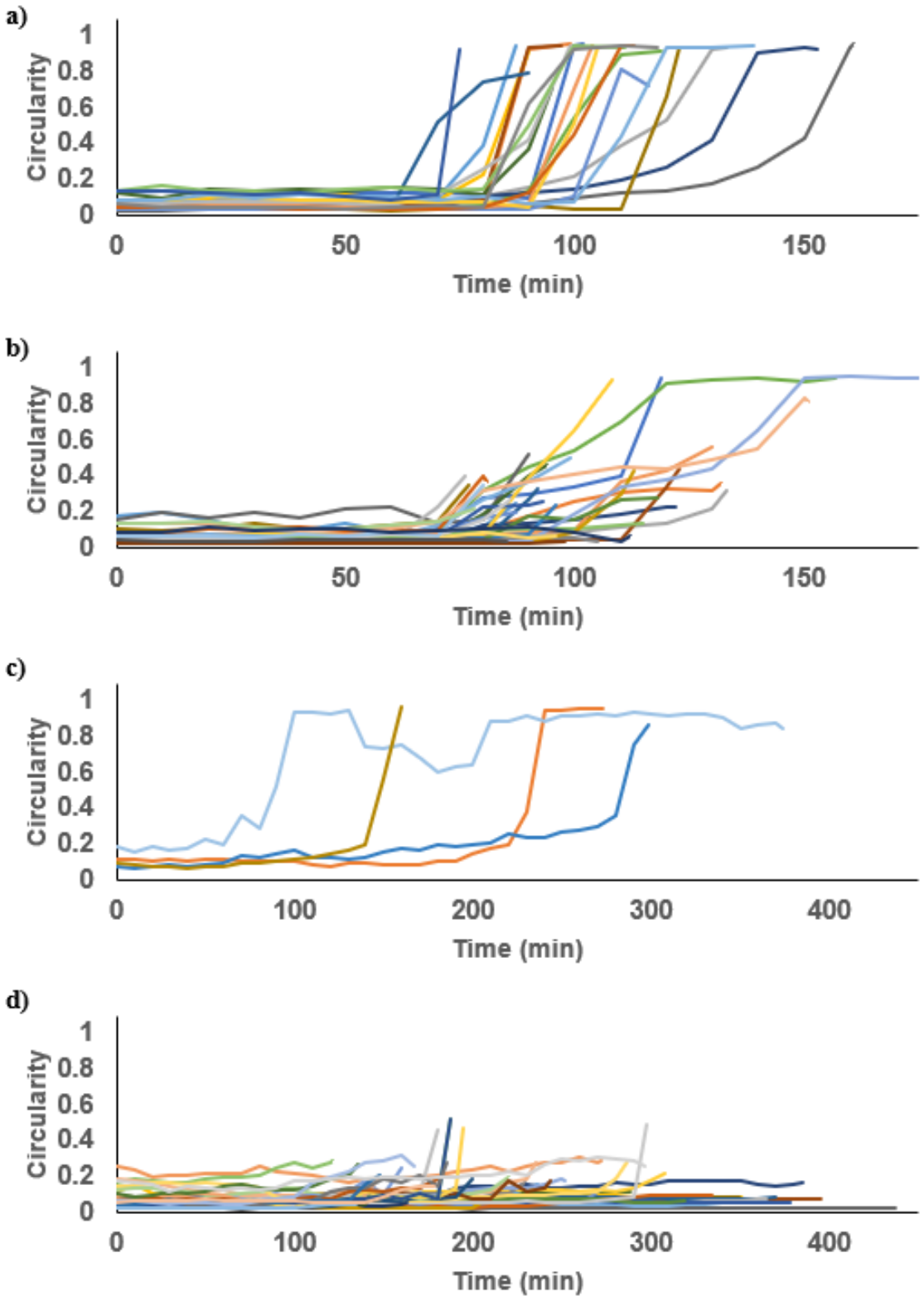

Figure 3.11. Sharp and gradual modes of death were isolated for small spacing parallel cells to identify further trends: a) PA14 sharp (N = 21), b) PA14 gradual (N = 33), c) PAO1 sharp (N = 4), d) PAO1 gradual (N = 47).

The final (i.e., at the time of death) circularity value was also gathered for each cell and plotted in Figure 3.12 for each morphology and bacteria strain combination. It is evident that for all morphologies, the average final circularity was smaller for PAO1 compared to that of PA14. This is consistent with the majority gradual cell death observed in cells interacting with PAO1, indicating that the cells undergo less change in shape (circularity) over time. Furthermore, four out of six identical morphologies carried a significant difference between bacteria strains: flat ($p < 0.0001$), spindle ($p < 0.0001$), parallel ($p < 0.0001$), and 20 μm ($p < 0.0001$) (i.e. flat PAO1 was significantly different than flat PA14). All levels of significance found using Tukey HSD can be seen in Table 3.2. Furthermore, Table 3.3 shows the average final circularity values and levels of significance for cells of all morphologies exposed to PA14 dying by sharp and gradual shape change to death. As expected, no significant differences arose between sharp death cells on any of the fiber configurations due to the stringent inclusionary criteria for sharp death categorization. In addition, none of the gradual death cells shared significant differences in final circularity values, except between cells on the 2D flat surface and 5 μm crosshatch. Lastly, Table 3.4 displays average final circularity values and levels of significance for cells of all morphologies exposed to PAO1 dying by only gradual shape change to death, due to the limitation in N values for PAO1 exposed cells with sharp deaths. Several levels of significance were found between cells of varied morphologies with 5 μm cells having the greatest average final circularity and the small spacing parallel cells having the smallest average final circularity. Time of cell death was similarly investigated by comparing sharp and gradual time to cell death for cells exposed to PA14 and gradual time to cell death for cells exposed to PAO1 (see Appendix A.2).

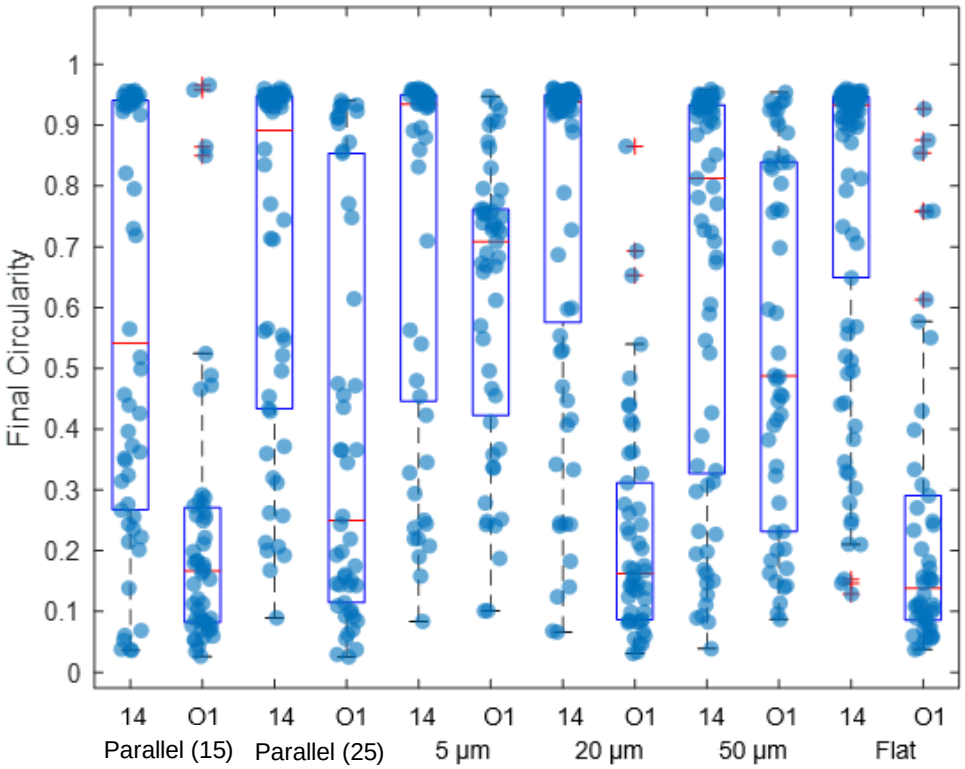

Figure 3.12. Final circularity values were compared across the following fibroblast cell morphologies treated with cytotoxic PA14 or invasive PAO1, respectively: parallel (15) (N = 54, 51), parallel (25) (N = 54, 50), 5 µm (N = 53, 51), 20 µm (N = 72, 50), 50 µm (N = 69, 50), and flat (N = 94, 50).

Table 3.2. Final circularity levels of significance for cells of all morphologies exposed to both PA14 and PAO1.

Strain/Morphology	Level						Average Final Circularity	Standard Error
PA14 Flat	A						0.78	0.031
PA14 20 µm	A	B					0.77	0.035
PA14 5 µm	A	B	C				0.73	0.041
PA14 Parallel (25)	A	B	C	D			0.70	0.041
PA14 50 µm	A	B	C	D			0.66	0.036
PAO1 5 µm		B	C	D			0.62	0.037
PA14 Parallel (15)			C	D	E		0.58	0.041
PAO1 50 µm				D	E		0.55	0.037
PAO1 Parallel (25)					E	F	0.41	0.037
PAO1 Flat						F	0.24	0.037
PAO1 Parallel (15)						F	0.23	0.037
PAO1 20 µm						F	0.23	0.037

Table 3.3. Final circularity levels of significance for cells of all morphologies exposed to PA14 dying by sharp and gradual shape changes to death.

Morphology	Level			Average Final Circularity	Standard Error
5 μm Sharp	A			0.93	0.026
20 μm Sharp	A			0.93	0.022
Flat Sharp	A			0.92	0.020
Parallel (15) Sharp	A			0.91	0.034
Parallel (25) Sharp	A			0.91	0.029
50 μm Sharp	A			0.90	0.025
Flat Gradual		B		0.48	0.029
Parallel (25) Gradual		B	C	0.43	0.032
Parallel (15) Gradual		B	C	0.37	0.027
50 μm Gradual		B	C	0.36	0.029
20 μm Gradual		B	C	0.34	0.035
5 μm Gradual			C	0.31	0.038

Table 3.4. Final circularity levels of significance for cells of all morphologies exposed to PAO1 dying by gradual shape change to death. Due to sparsity of sharp shape change to death, the corresponding data were excluded from the statistical analysis.

Morphology	Level				Average Final Circularity	Standard Error
5 μm Gradual	A				0.59	0.033
50 μm Gradual	A	B			0.46	0.035
Parallel (25) Gradual		B	C		0.32	0.035
20 μm Gradual			C	D	0.23	0.032
Flat Gradual			C	D	0.22	0.032
Parallel (15) Gradual				D	0.17	0.033

3.4 *P. aeruginosa* Strain Type and Cell Morphology Influence Migration Dynamics

Next, it was sought to determine whether the type of bacteria introduced influenced the dynamics of cell migration. First, an average migration speed was calculated for all cells migrating on parallel fibers with large and small spacing formations up until the initiation of cytoskeletal contraction, as values beyond this point were not representative of typical cell migration (Figure 3.13a). There was no statistically significant difference found between cells on small and large spacing parallel networks for the same bacteria types ($p > 0.05$). It was hypothesized that PA14

exposed cells may have slower speeds than those exposed to PAO1 due to the disparity in cytotoxic factors. However, PAO1 treated small spacing parallel cells were found to be significantly slower than both PA14 treated large spacing parallel cells ($p < 0.001$) and PA14 treated small spacing parallel cells ($p < 0.01$). The faster speeds of PA14 exposed cells may be as a result of the sudden change in cell morphology due to high levels of PA14 virulence as compared to the PAO1 exposed cells which have longer bacteria treatment times, resulting in decreased migration speeds. The speed of control cells was also obtained for cells on both parallel networks (Figure 3.13b). Due to sparsity of small spacing parallel control cells, the control data was excluded form statistical analysis. However, small (34.6 ± 10.4 μm/hr) and large (40.5 ± 17.4 μm/hr) spacing parallel morphology control cells were seen to have similar speed values to small (34.8 ± 16.1 μm/hr) and large (37.3 ± 12.0 μm/hr) spacing parallel morphology PA14 treated cells.

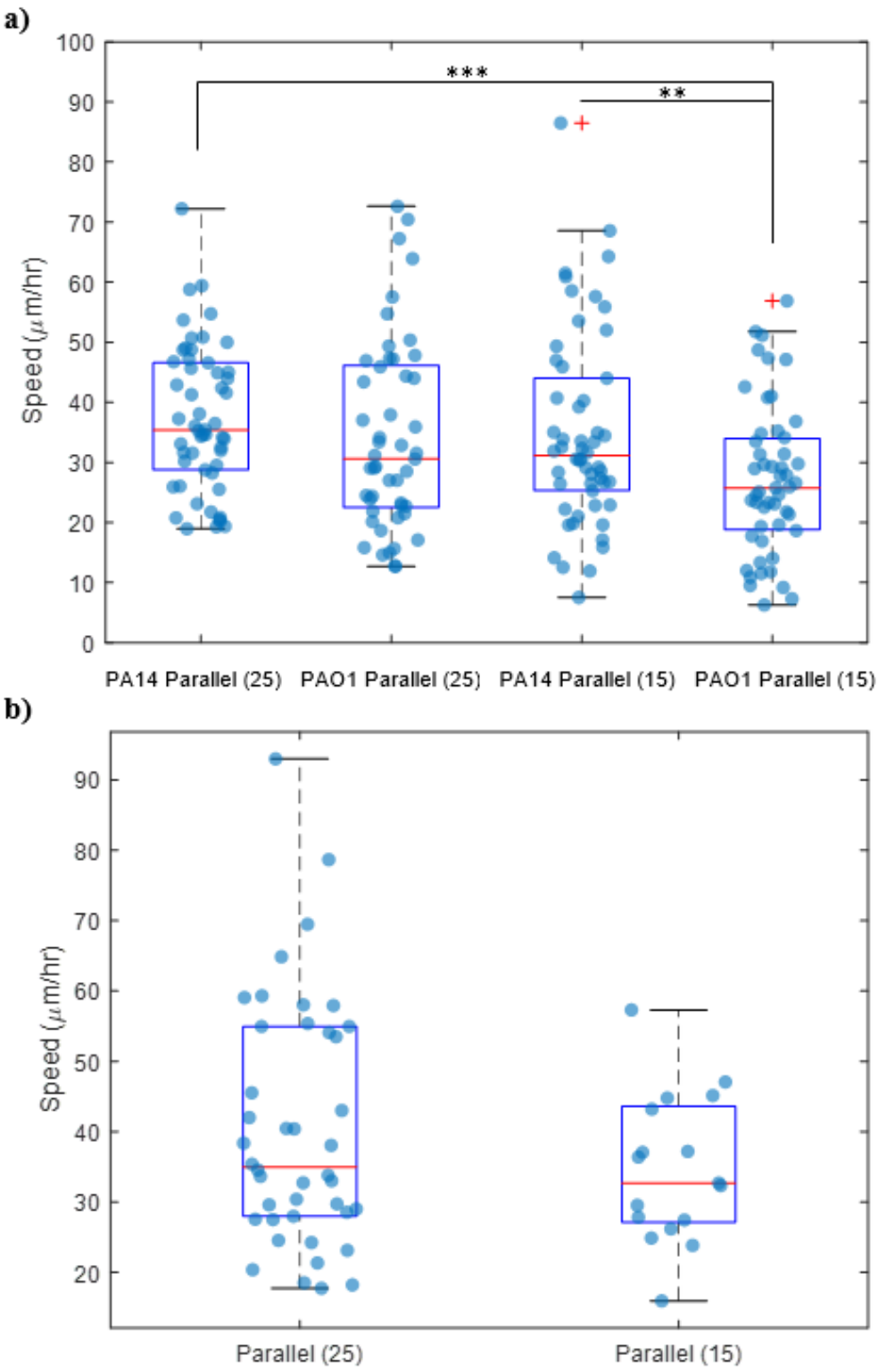

Figure 3.13. The speed of fibroblast cells migrating in a) large spacing parallel (PA14: N = 54, PAO1: N = 50) and small spacing parallel (PA14: N = 54, PAO1: N = 51) morphologies during PA14 and PAO1 invasion and in b) large spacing parallel (N = 42) and small spacing parallel (N = 17) morphologies with no bacteria (control). *** $p < 0.001$ and ** $p < 0.01$.

Persistence was also examined for cells migrating on parallel fibers with large and small spacing formations (Figure 3.14a). Similar to the trends seen for migration speed, persistence of small spacing parallel cells exposed to PAO1 was found to be significantly different from that of cells exposed to PA14 on the large and small spacing parallel fiber networks. However, in this instance, the largest statistically significant difference was seen between cells exposed to PAO1 on the large and small spacing parallel fiber configurations ($p < 0.001$). The persistence of control cells was also obtained for cells on both parallel networks (Figure 3.14b). Due to sparsity of small spacing parallel control cells, the control data was excluded form statistical analysis. However, small and large spacing parallel morphology control cells were seen to have greater average persistence values than all bacteria treated cells, with values of 0.53 ± 0.36, and 0.72 ± 0.30, respectively.

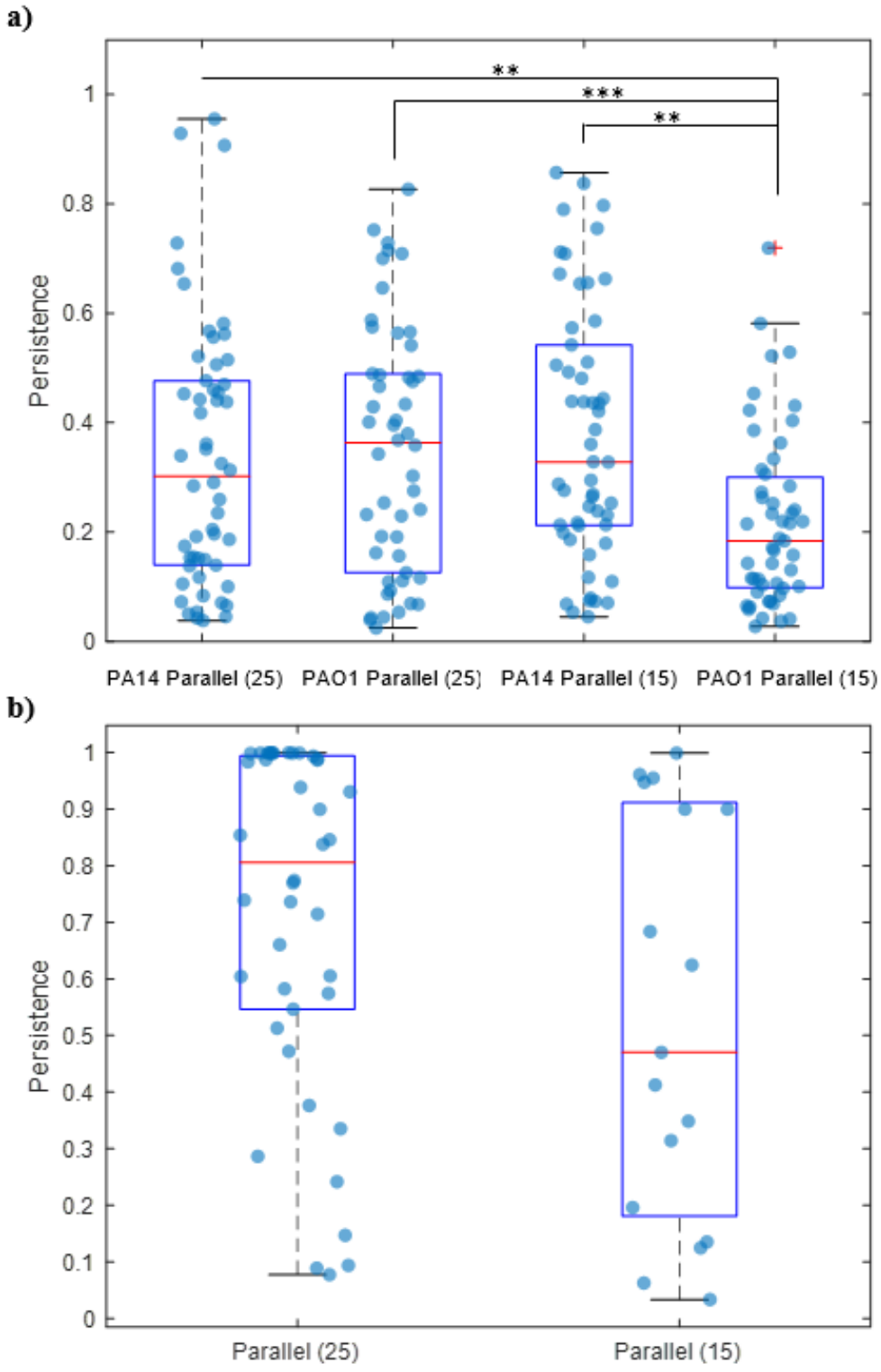

Figure 3.14. The persistence of cells migrating in a) large (PA14: N = 54, PAO1: N = 50) and small (PA14: N = 54, PAO1: N = 51) spacing parallel morphologies during PA14 and PAO1 invasion and b) large (N = 42) and small (N = 17) spacing parallel morphologies with no bacteria (control). (**p < 0.01, ***p < 0.001).

3.5 Contractile Cell Force Depreciates Over Time for Both *P. aeruginosa* Strains

Nanonet force microscopy was used to quantify changes in force exerted by the fibroblast cells over the course of bacterial invasion for both strains (Figure 3.15) (Sheets et al. 2016; Padhi, Hall, and Nain 2017). In both cases, forces fluctuated about an average value up until near complete loss of contractile force, wherein the fiber deflection could not be reliably measured. No significant difference was found between average force values for PA14 exposed cells and PAO1 exposed cells prior to relaxation ($p > 0.05$) (Figure 3.16). However, the time rate of change of force was found to be different. For cells exposed to PA14, a mix of rapid and gradual degradation in contractile force was observed (Figure 3.15a), whereas only gradual force degradation was observed in cells exposed to PAO1 (Figure 3.15b). This behavior is consistent with the breakdown of manner of death discussed previously, where cells exposed to PA14 are more likely to die by manner of sharp death than those exposed to PAO1, possibly due to loss of cytoskeletal contractility (Table 3.1). It was considered that force fluctuations seen in Figure 3.15 may be a result of active fluctuations observed in cytoskeletal networks. However, using microrheology experimentation, the frequency of nonequilibrium fluctuations of a remodeling cytoskeleton have been shown to be beyond the resolution of the force measurements in this experiment (Stuhrmann et al. 2012).

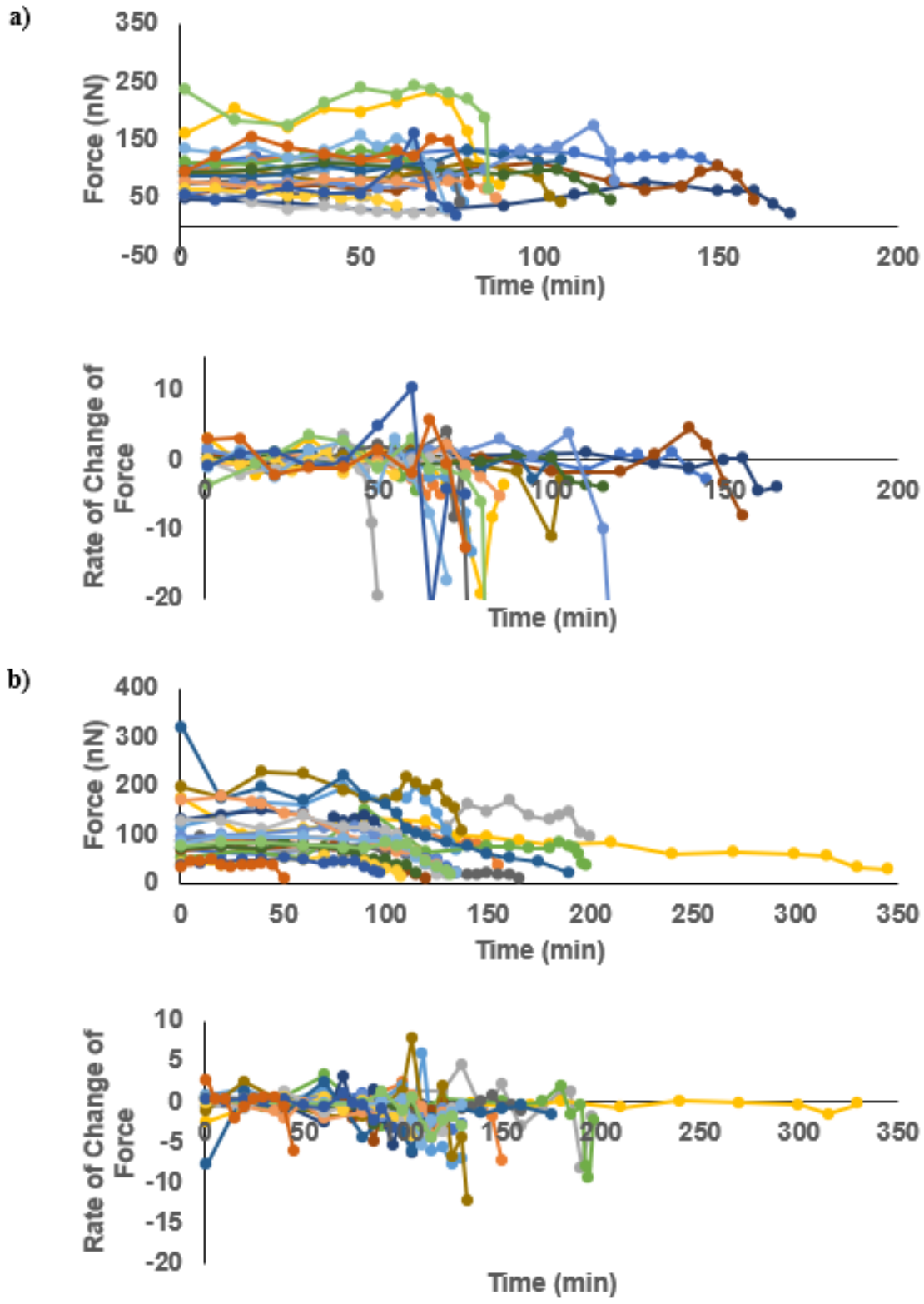

Figure 3.15. Force and rate of change of force were compared for cells exposed to a) PA14 (N = 20) and b) PAO1 (N = 20).

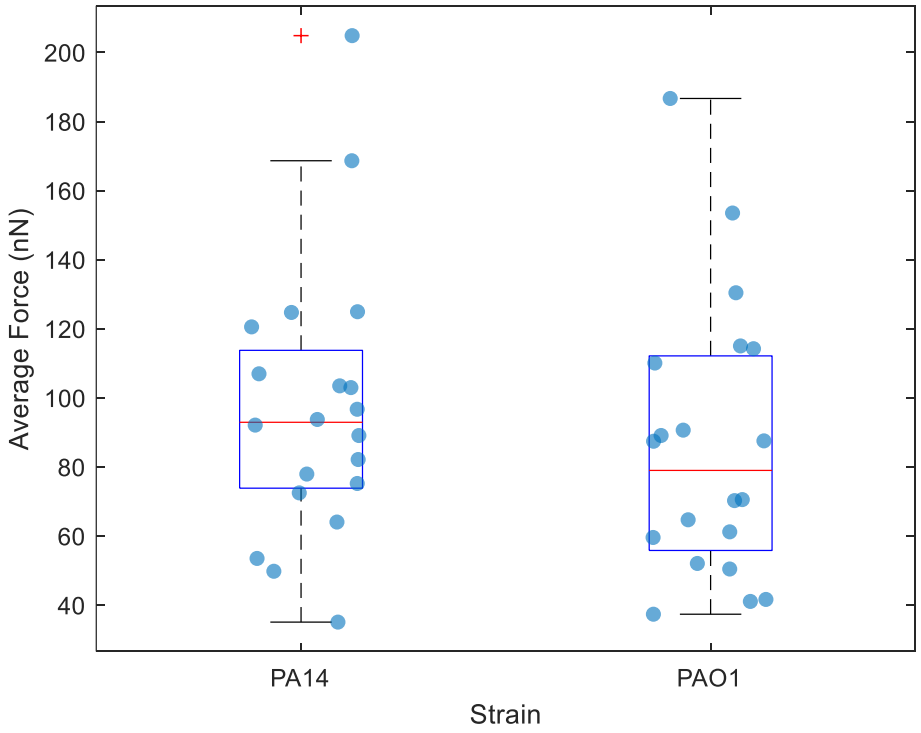

Figure 3.16. Average force values were accumulated for all cells and compared across PA14 (N = 20) and PAO1 (N = 20). No significant difference was found.

To ensure that changes in force were a result of bacteria introduction, force was measured for ten control cells in absence of bacteria. Figure 3.17 shows that the contractile force exerted by the control cells were time invariant over a period of 60 minutes, demonstrating that the fluctuations in force shown in Figure 3.15 were a function of bacterial colonization, not due the nature of the cell.

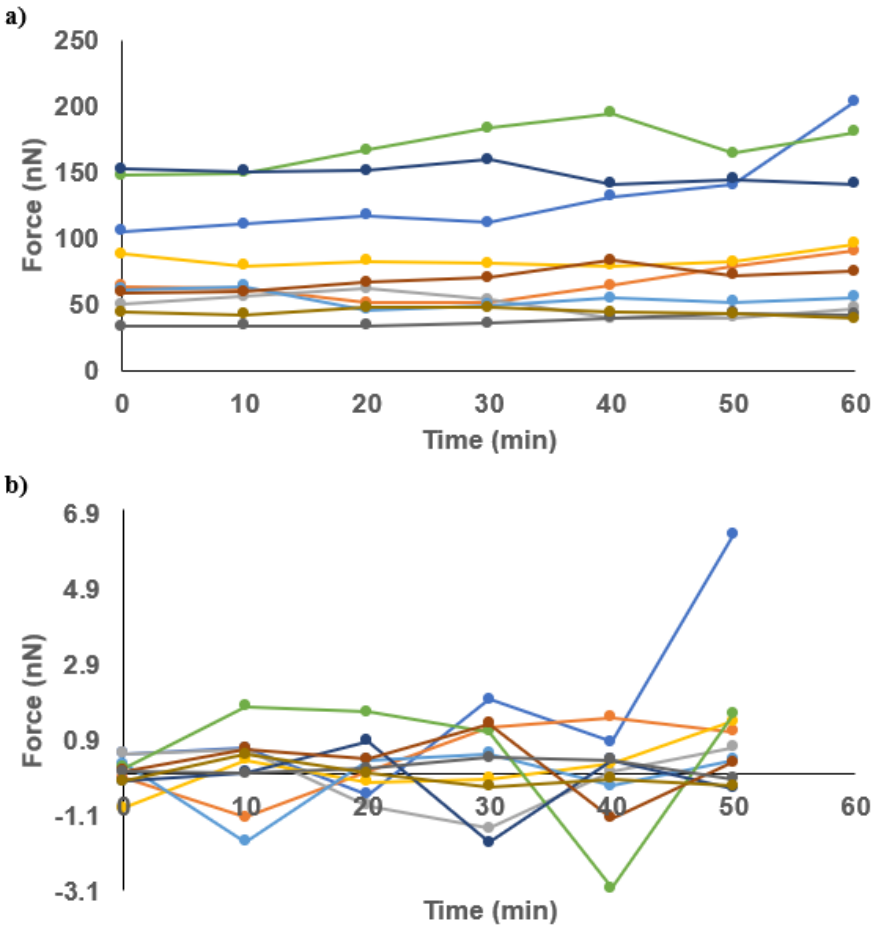

Figure 3.17. a) Force and b) rate of change of were measured for ten control cells without bacteria interaction. N = 10.

It was also observed that although PA14 and PAO1 induce significantly different cell death times for all cell morphologies (Figure 3.1b), the two strains of bacteria shared little difference in time of initial force depreciation. To quantitatively compare the cell force response to each of the two strains, the difference between time of death and initial force release was normalized by time of death and plotted in Figure 3.18. This parameter was significantly different ($p < 0.05$) between cells exposed to PA14 and PAO1, highlighting a larger difference in time between cell death and loss of force for cells exposed to PAO1.

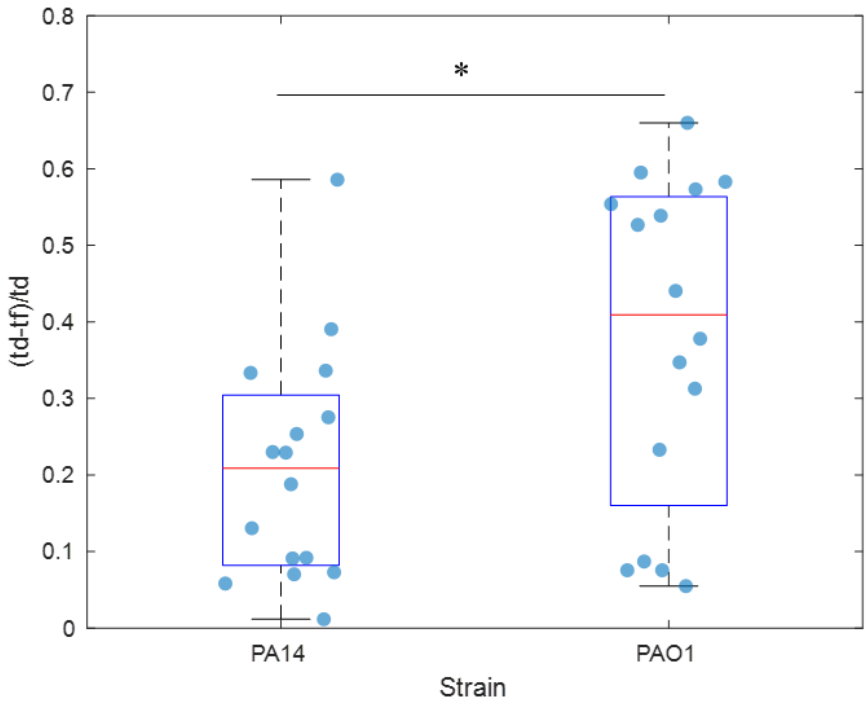

Figure 3.18. The time difference between death and initial loss of force was normalized by time of death and compared for cells exposed to PA14 (N = 16) and PAO1 (N = 16) (*p > 0.05).

3.6 *P. aeruginosa* Strain Type Influences Actin Stress Fiber Formation

Our observation in the temporal evolution of circularity and force suggested that changes to the actin stress fibers may be responsible for the observed behavior. Thus, immunofluorescence staining and confocal imaging was performed on control and bacteria treated cells in the parallel force fiber formation (Figure 3.18). Scaffold samples were prepared as described in Chapter 2.1. PA14 and PAO1 were introduced and allowed to interact with the fibroblasts for 45 and 65 minutes, respectively. These times were carefully chosen so images of elongated cells could be obtained while allowing for ample bacteria exposure to reveal potential alterations in the fibroblast cytoskeleton. In other words, fixation was performed when some of the seeded cells began to ball up, while others continued to stay elongated, to ensure the interaction time between fibroblasts and bacteria was sufficient. Subsequently, bacteria were removed and the fibroblasts were immediately

fixed. Representative images of maximum intensity projections are shown for the three cases in Figure 3.19. Unsurprisingly, control cells (Figure 3.19a) displayed the most prominent force transducing actin cables, providing an excellent comparison group for treated cells. Introduction of the cytotoxic strain PA14 (Figure 3.19b) led to a remarkable change in the actin stress fiber architecture evident by the formation of more actin punctae in contrast to prominent actin stress fibers seen in the control (Figure 3.19a) and PAO1 (Figure 3.19c) cases. It is speculated that these actin monometers congregated, not being able to form long actin filaments, as a response to the increased virulence of PA14 as compared to PAO1. By comparison, cells exposed to PAO1 (Figure 3.18c) were still able to maintain organized actin filaments over a longer bacteria treatment time. This is consistent with the breakdown of manner of death (Table 3.1) and time rate of change of force (Fig. 3.15) discussed previously; fibroblasts treated with PAO1 are more likely to die by gradual death than those treated with PA14, possibly due to their ability to better maintain actin integrity.

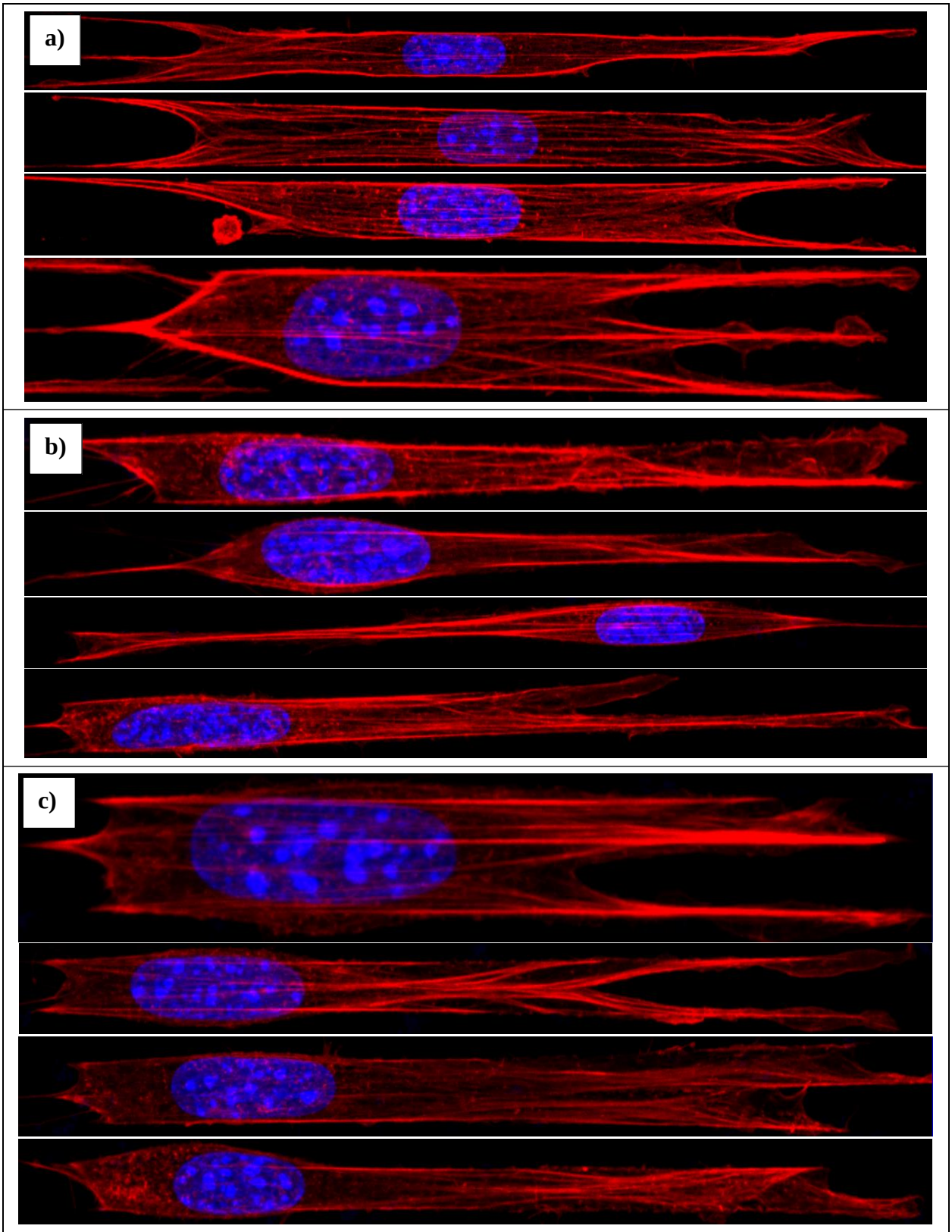

Figure 3.19. Confocal images were taken of actin structures for a) control cells, b) cells treated with PA14, and b) cells treated with PAO1.

3.7 Conclusions and Discussion

A study of NIH/3T3 fibroblast response to invasive (PA01) and cytotoxic (PA14) strains of *P. aeruginosa* bacteria was conducted to investigate the role of cell morphology and bacteria phenotype on cell response. The key distinguishing features of the two bacteria strains to be the increased ability of PA14 to quorum sense, and the presence of both T3SS complements, *exoS and exoT*, in PAO1 (T. G. Sana et al. 2021; Fleiszig et al. 1997). In using suspended nanofibers, we were able to recapitulate the ECM *in vitro* and quantify significant differences in cell behavior on five fiber formations and the 2D flat surface (control) for both bacteria strains. We were also able to correlate these changes with differing actin stress fiber configurations. The key findings of our research are:

Firstly, time to cell death was found to be independent of cell morphology for both PAO1, the invasive strain, and PA14, the cytotoxic strain. However, bacterial phenotype (cytotoxic vs. invasive) was found to have a significant effect on cell death time across all cell morphologies, as cells treated with PAO1 took 2.5× longer to die than those treated with PA14 ($p < 0.0001$).

Next, fiber architecture was shown to modulate cell spread area. Cells on the 2D flat surface, 50 μm mesh, and 20 μm mesh all produced spread morphologies whereas cells on parallel fibers with large spacing, parallel fibers with small spacing, and 5 μm mesh produced elongated morphologies. Altogether, spread area results demonstrated our ability to recapitulate *in vivo* morphologies seen in different layers of the dermis (Novotny and Gnoth 1991). Quantitatively, cells on the 2D flat surface had the largest initial spread area while cells on the dense crosshatch networks (5 μm) and on the parallel fibers with large spacing (25 μm) had the smallest spread area ($p > 0.05$). Similarly, no significant difference was found between initial spread area values for cells on parallel fibers with small spacing (15 μm) and the intermediate spaced mesh (20 μm) ($p > 0.05$). While cell spread area describes cell size on different substrate types, it does not describe cell shape. In other words,

two cells could have closely similar spread areas but distinctly different morphologies. Thus, we also examined the role of substrate on cell circularity. We found that fiber configurations also modulated cell circularity. Similarly elongated small and large spacing parallel cells had significantly lower initial circularity values than cells of all other morphologies whereas cells on the 5 μm mesh produced comparatively high circularity values. These initial circularity values provide insight into the differing configuration of the actin cytoskeleton on various fiber networks. Most importantly, two modes of death, sharp and gradual, were identified and classified based on rate of change of circularity and maximum circularity values. The manner of death was found to be dependent upon cell morphology and strain of bacteria. When interacting with the PA14 strain, Fibroblasts on the 20 μm spaced mesh died by means of a sharp death 72% of the time whereas cells in the small spacing parallel morphology only died by means of a sharp death 39% of the time. In contrast, cells exposed to PAO1 were more likely to die by gradual death for all morphologies, 20 μm showing the greatest probability with 100% gradual deaths. Lastly, all cell morphologies exposed to PAO1 had smaller final circularity values than those exposed to PA14.

Next, migration dynamics were shown to be dependent on morphology and strain of bacteria. PAO1 treated small spacing parallel cells were found to be significantly slower than both PA14 treated large spacing parallel cells ($p < 0.001$) and PA14 treated small spacing parallel cells ($p < 0.01$), while the migration speed of PAO1 treated large spacing cells was not statistically significantly different from the other three groups. However, persistence of PAO1 exposed small spacing parallel cells was found to be not only significantly different from that of PA14 treated large and small spacing parallel cells ($p < 0.01$) but also from PAO1 exposed large spacing parallel cells ($p < 0.001$).

Forces exerted by fibroblasts on 200 nm diameter fibers were quantified and shown to stay consistent between PAO1 and PA14 exposed cells ($p > 0.05$), up until a point of force fiber relaxation. The degradation of the contractile force upon exposure to PA14 occurred sharply or gradually, but only occurred gradually for PAO1 exposed cells. By comparison, control cells without bacteria interaction did not exhibit any significant degradation in force over time. Finally, a significantly larger difference in time between cell death and loss of force for cells exposed to PAO1 was noted ($p < 0.05$).

Lastly, using immunofluorescence staining, actin cables were found to be most prominent in control and PAO1 treated cells while actin of fibroblasts treated to PA14 was characterized by punctae and lesser defined stress fibers, potentially connecting changes in cell cytoskeleton to behaviors reported above.

Chapter 4. Conclusions and Future Works

The goals of this thesis were to recapitulate fibroblast morphologies seen *in vivo* and investigate how cytotoxic and invasive strains of *P. aeruginosa* influence cell morphodynamics. To accomplish these goals, three types of nanofiber coated scaffolds were fabricated, platforms which allowed us to quantify changes in cell morphology, migration, and force, while qualitatively comparing actin networks over the course of PA14 and PAO1 invasion. This chapter summarizes conclusions drawn from our findings, discusses the importance of our work to the scientific community, and reflects on limitations of the current study that elucidate potential future directions for fibroblast invasion assays.

4.1 Summary of Conclusions

The suspended nanofibers fabricated using the STEP method allowed us to achieve repeatable fiber spacing and diameter to test our hypotheses, that fiber network configuration and strain of bacteria play a role in changing cell morphodynamics. Firstly, cell death time was gathered for cells of all six morphologies and was confirmed to be 2.5x longer for cells exposed to PAO1 than PA14 (Figure 3.1). Unsurprisingly, when comparing cell spread area, 2D flat cells were significantly larger than cells of any other morphology while large spacing parallel and 5 μm cells were significantly smaller (Figure 3.3). As expected, elongated small and large spacing parallel cells shared no significant difference in initial circularity while 5 μm cells carried large circularity values (Figure 3.4). Significantly, two modes of fibroblast death, sharp and gradual, were identified and compared for each morphology bacteria strain combination (Table 3.1). Cells on the intermediate spaced mesh were the most likely to die by sharp death when exposed to PA14, however, by contrast, no cells on the intermediate spaced mesh died by sharp death when exposed to PAO1. In fact, cells of all morphologies treated with PAO1 were more likely to die by means

of gradual death and carry smaller final circularity values when compared to those treated with PA14. Using migration scaffolds, PAO1 cells were found to be significantly slower than both types of migratory cells exposed to PA14 and significantly less persistent than both PA14 categories as well as PAO1 large spacing parallel cells (Figure 3.13, 3.14). Next, using force scaffolds, the magnitude of cell force exertion was found to be similar for cells exposed to both strains of bacteria, until a point of force fiber relaxation at which PA14 exposed cells were more likely to quickly release fibers, sharply depreciating force (Figure 3.15). Lastly, actin stress fibers were shown to be less prominent in cells treated to PA14 as compared to control and PAO1 treated cells.

4.2 Significance of Results

Fibroblast interaction with *P. aeruginosa* is important to study because of its relevance in hospital acquired dermal infections. *P. aeruginosa* is most commonly associated with wound infections or lung infections such as pneumonia. Thus, most literature focuses on the interaction between *P. aeruginosa* and epithelial cells in the outmost layer of the skin or airway epithelial cells. While epithelial cells and fibroblasts are both eukaryotic cells and share many commonalities, they also differ in many ways, such as type and function of cell surface receptors. Difference in cell receptors, for example, may elucidate different mechanisms used by *P. aeruginosa* to colonize fibroblasts as compared to mechanisms which have already been discovered for colonizing epithelial cells. Thus, it is important to continue investigating fibroblast interaction with *P. aeruginosa* to aid in the fundamental understanding of wound invasion. Not only does our study provide insight into fibroblast response to invasion by quantifying changes in cell morphodynamics, but it utilizes a fibrous platform to recapitulate the ECM environment and fibroblast morphology representative of conditions *in vivo.*

4.3 Limitations and Future Works

Although this study was a great start in understanding the interactions between *P. aeruginosa* and fibroblasts, there are still limitations that exist which may drive potential for future works. The greatest limitation of this thesis work was the inability to count the number of bacteria attached to each analyzable fibroblast. Initially, fluorescent imaging was used to identify PA14 mKO cells more easily in the hopes of quantifying how many bacteria were attached to each fibroblast (see Appendix A.1). However, *P. aeruginosa* quickly clumped as they grew in the nutrient rich cell media, making it hard to count the number of bacteria in each clump. In order to improve bacteria counting techniques, flow cells may be implemented for the continuous removal of planktonic bacteria. With the addition of bacteria counts to these assays, a relationship between mode of death (sharp vs. gradual) and number of bacteria attached may be identified or ruled out. Several other relationships could also be explored such as the relationship between magnitude of fibroblast force exertion and number of bacteria attached. In addition, this work may benefit from a quantitative assay of defining cell death by using fluorescent reporters for activation of apoptosis pathway, such as caspase 3/7. This investigation will include developing a calibration curve to establish dependency between intensity of fluorescent signal and cell shape. Another limitation of the study was the absence of live actin imaging, limiting actin structure visualization to one period in time. By improving invasion assay imaging techniques, such as using confocal imaging as opposed to optical microscopy, actin structure can be visualized over the course of invasion. Another future works may involve running the same assays with a human fibroblast line to ensure that cell behaviors remain constant for fibroblasts of different animal origins. In addition, different mutants of *P. aeruginosa*, such as mutants in the T2SS and T3SS machinery, may be used to highlight the importance of various *P. aeruginosa* virulence factors in changing cell morphodynamics. Lastly, pharmacological treatments of fibroblast cytoskeletal components such as actin may elucidate how

a compromised cytoskeleton may affect fibroblast susceptibility to bacterial invasion.

References

Abercrombie, M., Joan E.M. Heaysman, and Susan M. Pegrum. 1971. “The Locomotion of Fibroblasts in Culture.” *Experimental Cell Research*. https://doi.org/10.1016/0014-4827(71)90420-4.

Adamo, Robert, Sach Sokol, Grace Soong, Marisa I. Gomez, and Alice Prince. 2004. “Pseudomonas Aeruginosa Flagella Activate Airway Epithelial Cells through AsialoGM1 and Toll-like Receptor 2 as Well as Toll-like Receptor 5.” *American Journal of Respiratory Cell and Molecular Biology*. https://doi.org/10.1165/rcmb.2003-0260OC.

Alberts, Bruce, Alexander Johnson, Julian Lewis, Martin Raff, Roberts Keith, and Peter Walter. 2014. “Fibroblasts and Their Transformations: The Connective-Tissue Cell Family.” *Molecular Biology of the Cell*. https://doi.org/10.1016/j.jid.2017.10.012.

Arora, Shiwani K., Bruce W. Ritchings, Ernesto C. Almira, Stephen Lory, and Reuben Ramphal. 1998. “The Pseudomonas Aeruginosa Flagellar Cap Protein, FliD, Is Responsible for Mucin Adhesion.” *Infection and Immunity*. https://doi.org/10.1128/iai.66.3.1000-1007.1998.

Barbieri, J. T., and J. Sun. 2004. “Pseudomonas Aeruginosa ExoS and ExoT.” *Reviews of Physiology, Biochemistry and Pharmacology*. https://doi.org/10.1007/s10254-004-0031-7.

Beaufort, Nathalie, Elisabeth Corvazier, Saouda Mlanaoindrou, Sophie de Bentzmann, and Dominique Pidard. 2013. “Disruption of the Endothelial Barrier by Proteases from the Bacterial Pathogen Pseudomonas Aeruginosa: Implication of Matrilysis and Receptor Cleavage.” *PLoS ONE*. https://doi.org/10.1371/journal.pone.0075708.

Bradley, David E. 1972. “Evidence for the Retraction of Pseudomonas Aeruginosa RNA Phage Pili.” *Biochemical and Biophysical Research Communications*. https://doi.org/10.1016/S0006-291X(72)80021-4.

Bucior, Iwona, Julia F. Pielage, and Joanne N. Engel. 2012. “Pseudomonas Aeruginosa Pili and Flagella Mediate Distinct Binding and Signaling Events at the Apical and Basolateral Surface of Airway Epithelium.” *PLoS Pathogens*. https://doi.org/10.1371/journal.ppat.1002616.

CDC. 2019. “Antibiotic Resistance Threats in the United States, 2019, Atlanta, GA: U.S. Department of Health and Human Services.” *Center for Disease Control and Prevention*. https://doi.org/CS239559-B.

Church, Deirdre, Sameer Elsayed, Owen Reid, Brent Winston, and Robert Lindsay. 2006. “Burn Wound Infections.” *Clinical Microbiology Reviews*. https://doi.org/10.1128/CMR.19.2.403-434.2006.

Comolli, James C., Leslie L. Waite, Keith E. Mostov, and Joanne N. Engel. 1999. “Pili Binding to Asialo-GM1 on Epithelial Cells Can Mediate Cytotoxicity or Bacterial Internalization by Pseudomonas Aeruginosa.” *Infection and Immunity*. https://doi.org/10.1128/iai.67.7.3207-3214.1999.

Costa, Tiago R.D., Catarina Felisberto-Rodrigues, Amit Meir, Marie S. Prevost, Adam Redzej, Martina Trokter, and Gabriel Waksman. 2015. “Secretion Systems in Gram-Negative

Bacteria: Structural and Mechanistic Insights." *Nature Reviews Microbiology*. https://doi.org/10.1038/nrmicro3456.

Craig, Lisa, Katrina T. Forest, and Berenike Maier. 2019. "Type IV Pili: Dynamics, Biophysics and Functional Consequences." *Nature Reviews Microbiology*. Nature Publishing Group. https://doi.org/10.1038/s41579-019-0195-4.

Dacheux, Denis, Julien Goure, Jacqueline Chabert, Yves Usson, and Ina Attree. 2001. "Pore-Forming Activity of Type III System-Secreted Proteins Leads to Oncosis of Pseudomonas Aeruginosa-Infected Macrophages." *Molecular Microbiology*. https://doi.org/10.1046/j.1365-2958.2001.02368.x.

Dasgupta, Nandini, Shiwani K. Arora, and Reuben Ramphal. 2004. "The Flagellar System of Pseudomonas Aeruginosa." In *Pseudomonas*. https://doi.org/10.1007/978-1-4419-9086-0_22.

Doyle, Andrew D., Francis W. Wang, Kazue Matsumoto, and Kenneth M. Yamada. 2009. "One-Dimensional Topography Underlies Three-Dimensional Fi Brillar Cell Migration." *Journal of Cell Biology*. https://doi.org/10.1083/jcb.200810041.

Driscoll, James A., Steven L. Brody, and Marin H. Kollef. 2007. "The Epidemiology, Pathogenesis and Treatment of Pseudomonas Aeruginosa Infections." *Drugs*. https://doi.org/10.2165/00003495-200767030-00003.

Emam, Aufaugh, Analyn R. Yu, Hyun Joo Park, Radhia Mahfoud, Julianne Kus, Lori L. Burows, and Clifford A. Lingwood. 2006. "Laboratory and Clinical Pseudomonas Aeruginosa Strains Do Not Bind Glycosphingolipids in Vitro or during Type IV Pili-Mediated Initial Host Cell Attachment." *Microbiology*. https://doi.org/10.1099/mic.0.28863-0.

Feldman, Matthew, Ruth Bryan, Sujatha Rajan, Lee Scheffler, Steven Brunnert, Hope Tang, and Alice Prince. 1998. "Role of Flagella in Pathogenesis of Pseudomonas Aeruginosa Pulmonary Infection." *Infection and Immunity*. https://doi.org/10.1128/iai.66.1.43-51.1998.

Fleiszig, Suzanne M.J., Jeanine P. Wiener-Kronish, Hiroshi Miyazaki, V. Vallas, Keith E. Mostov, Daniel Kanada, Teiji Sawa, T. S.Benedict Yen, and Dara W. Frank. 1997. "Pseudomonas Aeruginosa-Mediated Cytotoxicity and Invasion Correlate with Distinct Genotypes at the Loci Encoding Exoenzyme S." *Infection and Immunity* 65 (2). https://doi.org/10.1128/iai.65.2.579-586.1997.

Fleiszig, Suzanne M.J., Tanweer S. Zaidi, Michael J. Preston, Martha Grout, David J. Evans, and Gerald B. Pier. 1996. "Relationship between Cytotoxicity and Corneal Epithelial Cell Invasion by Clinical Isolates of Pseudomonas Aeruginosa." *Infection and Immunity* 64 (6): 2288–94. https://doi.org/10.1128/iai.64.6.2288-2294.1996.

Forrest, L. 1983. "Current Concepts in Soft Connective Tissue Wound Healing." *British Journal of Surgery*. https://doi.org/10.1002/bjs.1800700302.

Golovkine, Guillaume, Eric Faudry, Stéphanie Bouillot, Sylvie Elsen, Ina Attrée, and Philippe Huber. 2016. "Pseudomonas Aeruginosa Transmigrates at Epithelial Cell-Cell Junctions, Exploiting Sites of Cell Division and Senescent Cell Extrusion." *PLoS Pathogens* 12 (1).

https://doi.org/10.1371/journal.ppat.1005377.

Green, Erin R., and Joan Mecsas. 2016. “Bacterial Secretion Systems: An Overview.” *Microbiology Spectrum* 4 (1). https://doi.org/10.1128/microbiolspec.vmbf-0012-2015.

Harrison-Balestra, Catherine, Alejandro L. Cazzaniga, Stephen C. Davis, and Patricia M. Mertz. 2003. “A Wound-Isolated Pseudomonas Aeruginosa Grows a Biofilm in Vitro within 10 Hours and Is Visualized by Light Microscopy.” *Dermatologic Surgery*. https://doi.org/10.1046/j.1524-4725.2003.29146.x.

Hauser, Alan R. 2009. “The Type III Secretion System of Pseudomonas Aeruginosa: Infection by Injection.” *Nature Reviews Microbiology*. https://doi.org/10.1038/nrmicro2199.

Hoge, R, A Pelzer, F Rosenau, and S Wilhelm. 2010. “Weapons of a Pathogen: Proteases and Their Role in Virulence of Pseudomonas Aeruginosa.” *Current Research, Technology and Education Topics in Applied Microbiology and Microbial Biotechnology* 45.

Iwasa, Hiroaki, Jiahuai Han, and Fuyuki Ishikawa. 2003. “Mitogen-Activated Protein Kinase P38 Defines the Common Senescence-Signalling Pathway.” *Genes to Cells* 8 (2). https://doi.org/10.1046/j.1365-2443.2003.00620.x.

Jacobs, Christopher R., Hayden Huang, and Ronald Y. Kwon. 2012. *Introduction to Cell Mechanics and Mechanobiology*. *Introduction to Cell Mechanics and Mechanobiology*. https://doi.org/10.1201/9781135042653.

Jana, Aniket, Intawat Nookaew, Jugroop Singh, Bahareh Behkam, Aime T. Franco, and Amrinder S. Nain. 2019. “Crosshatch Nanofiber Networks of Tunable Interfiber Spacing Induce Plasticity in Cell Migration and Cytoskeletal Response.” *FASEB Journal*. https://doi.org/10.1096/fj.201900131R.

Kato, Junichi, Hye Eun Kim, Noboru Takiguchi, Akio Kuroda, and Hisao Ohtake. 2008. “Pseudomonas Aeruginosa as a Model Microorganism for Investigation of Chemotactic Behaviors in Ecosystem.” *Journal of Bioscience and Bioengineering*. https://doi.org/10.1263/jbb.106.1.

Korotkov, Konstantin V., Maria Sandkvist, and Wim G.J. Hol. 2012. “The Type II Secretion System: Biogenesis, Molecular Architecture and Mechanism.” *Nature Reviews Microbiology*. https://doi.org/10.1038/nrmicro2762.

LAUTROP, H. 1962. “Bacterium Anitratum Transferred to the Genus Cytophaga.” *Acta Pathologica et Microbiologica Scandinavica. Supplement*. https://doi.org/10.1099/0096266x-11-3-107.

Magariyama, Y., S. Sugiyama, K. Muramoto, Y. Maekawa, I. Kawagishi, Y. Imae, and S. Kudo. 1994. “Very Fast Flagellar Rotation [11].” *Nature*. https://doi.org/10.1038/371752b0.

Mattick, John S., Cynthia B. Whitchurch, and Richard A. Alm. 1996. “The Molecular Genetics of Type-4 Fimbriae in Pseudomonas Aeruginosa - A Review.” *Gene*. https://doi.org/10.1016/S0378-1119(96)00441-6.

Michalska, Marta, and Philipp Wolf. 2015. “Pseudomonas Exotoxin A: Optimized by Evolution for Effective Killing.” *Frontiers in Microbiology*.

https://doi.org/10.3389/fmicb.2015.00963.

Mikkelsen, Helga, Rachel McMullan, and Alain Filloux. 2011. “The Pseudomonas Aeruginosa Reference Strain PA14 Displays Increased Virulence Due to a Mutation in LadS.” *PLoS ONE* 6 (12). https://doi.org/10.1371/journal.pone.0029113.

Missirlis, Dimitris, Tamás Haraszti, Horst Kessler, and Joachim P. Spatz. 2017. “Fibronectin Promotes Directional Persistence in Fibroblast Migration through Interactions with Both Its Cell-Binding and Heparin-Binding Domains.” *Scientific Reports*. https://doi.org/10.1038/s41598-017-03701-0.

Miyazaki, S., T. Matsumoto, K. Tateda, A. Ohno, and K. Yamaguchi. 1995. “Role of Exotoxin A in Inducing Severe Pseudomonas Aeruginosa Infections in Mice.” *Journal of Medical Microbiology* 43 (3). https://doi.org/10.1099/00222615-43-3-169.

Moradali, M. Fata, Shirin Ghods, and Bernd H.A. Rehm. 2017. “Pseudomonas Aeruginosa Lifestyle: A Paradigm for Adaptation, Survival, and Persistence.” *Frontiers in Cellular and Infection Microbiology*. https://doi.org/10.3389/fcimb.2017.00039.

Morihara, Kazuyuki, Hiroshige Tsuzuki, Tatsushi Oka, Hideo Inoue, and Mitsuo Ebata. 1965. “Pseudomonas Aeruginosa Elastase.” *The Journal of Biological Chemistry*.

Muller, Michael, Zhe Li, and Peter K.M. Maitz. 2009. “Pseudomonas Pyocyanin Inhibits Wound Repair by Inducing Premature Cellular Senescence: Role for P38 Mitogen-Activated Protein Kinase.” *Burns* 35 (4). https://doi.org/10.1016/j.burns.2008.11.010.

Nain, Amrinder S., Metin Sitti, Annette Jacobson, Tomasz Kowalewski, and Cristina Amon. 2009. “Dry Spinning Based Spinneret Based Tunable Engineered Parameters (STEP) Technique for Controlled and Aligned Deposition of Polymeric Nanofibers.” *Macromolecular Rapid Communications*. https://doi.org/10.1002/marc.200900204.

Novotny, G. E.K., and E. Gommert-Novotny. 1990. “A Simple Procedure for Demonstrating the Overall Morphology of Fibroblasts in Routine Histological Preparations of Adult Tissues, Using Silver Impregnation.” *Journal of Microscopy* 159 (1). https://doi.org/10.1111/j.1365-2818.1990.tb03023.x.

Padhi, Abinash, Alex Hall, and Amrinder S. Nain. 2017. “Nanonet Force Microscopy.” *Biophysical Journal* 112 (3): 271a. https://doi.org/10.1016/j.bpj.2016.11.1469.

Paranchych, William, and Laura S. Frost. 1988. “The Physiology and Biochemistry of Pili.” *Advances in Microbial Physiology*. https://doi.org/10.1016/S0065-2911(08)60346-X.

Pastor, Alexandrine, Jacqueline Chabert, Mathilde Louwagie, Jerôme Garin, and Ina Attree. 2005. “PscF Is a Major Component of the Pseudomonas Aeruginosa Type III Secretion Needle.” *FEMS Microbiology Letters* 253 (1): 95–101. https://doi.org/10.1016/j.femsle.2005.09.028.

Petrie, Ryan J., Núria Gavara, Richard S. Chadwick, and Kenneth M. Yamada. 2012. “Nonpolarized Signaling Reveals Two Distinct Modes of 3D Cell Migration.” *Journal of Cell Biology*. https://doi.org/10.1083/jcb.201201124.

Russell, Alistair B., Rachel D. Hood, Nhat Khai Bui, Michele Leroux, Waldemar Vollmer, and

Joseph D. Mougous. 2011. “Type VI Secretion Delivers Bacteriolytic Effectors to Target Cells.” *Nature* 475 (7356). https://doi.org/10.1038/nature10244.

Sana, T. G., R. Lomas, M. R. Gimenez, A. Laubier, C. Soscia, C. Chauvet, A. Conesa, R. Voulhoux, B. Ize, and S. Bleves. 2021. “Differential Modulation of Quorum Sensing Signaling through QslA in Pseudomonas Aeruginosa Strains PAO1 and PA14.” *Journal of Bacteriology* 201 (21). https://doi.org/10.1128/JB.00362-19.

Sana, Thibault G., Christoph Baumann, Andreas Merdes, Chantal Soscia, Thomas Rattei, Abderrahman Hachani, Cerith Jones, et al. 2015. “Internalization of Pseudomonas Aeruginosa Strain PAO1 into Epithelial Cells Is Promoted by Interaction of a T6SS Effector with the Microtubule Network.” *MBio* 6 (3). https://doi.org/10.1128/mBio.00712-15.

Sauvonnet, Nathalie, Guillaume Vignon, Anthony P. Pugsley, and Pierre Gounon. 2000. “Pilus Formation and Protein Secretion by the Same Machinery in Escherichia Coli.” *EMBO Journal* 19 (10). https://doi.org/10.1093/emboj/19.10.2221.

Schmidtchen, Artur, Elisabet Holst, Hans Tapper, and Lars Björck. 2003. “Elastase-Producing Pseudomonas Aeruginosa Degrade Plasma Proteins and Extracellular Products of Human Skin and Fibroblasts, and Inhibit Fibroblast Growth.” *Microbial Pathogenesis*. https://doi.org/10.1016/S0882-4010(02)00197-3.

Semmler, Annalese B.T., Cynthia B. Whitchurch, and John S. Mattick. 1999. “A Re-Examination of Twitching Motility in Pseudomonas Aeruginosa.” *Microbiology*. https://doi.org/10.1099/00221287-145-10-2863.

Sheets, Kevin, Ji Wang, Wei Zhao, Rakesh Kapania, and Amrinder S. Nain. 2016. “Nanonet Force Microscopy for Measuring Cell Forces.” *Biophysical Journal*. https://doi.org/10.1016/j.bpj.2016.05.031.

Stuhrmann, Björn, Marina Soares E Silva, Martin Depken, Frederick C. MacKintosh, and Gijsje H. Koenderink. 2012. “Nonequilibrium Fluctuations of a Remodeling in Vitro Cytoskeleton.” *Physical Review E - Statistical, Nonlinear, and Soft Matter Physics* 86 (2). https://doi.org/10.1103/PhysRevE.86.020901.

Thuenauer, Roland, Alessia Landi, Anne Trefzer, Silke Altmann, Sarah Wehrum, Thorsten Eierhoff, Britta Diedrich, et al. 2020. “The Pseudomonas Aeruginosa Lectin Lecb Causes Integrin Internalization and Inhibits Epithelial Wound Healing.” *MBio*. https://doi.org/10.1128/mBio.03260-19.

Tomasek, James J., Giulio Gabbiani, Boris Hinz, Christine Chaponnier, and Robert A. Brown. 2002. “Myofibroblasts and Mechano: Regulation of Connective Tissue Remodelling.” *Nature Reviews Molecular Cell Biology*. https://doi.org/10.1038/nrm809.

Vater, Svenja M., Sebastian Weiße, Stojan Maleschlijski, Carmen Lotz, Florian Koschitzki, Thomas Schwartz, Ursula Obst, and Axel Rosenhahn. 2014. “Swimming Behavior of Pseudomonas Aeruginosa Studied by Holographic 3D Tracking.” *PLoS ONE*. https://doi.org/10.1371/journal.pone.0087765.

Wu, Weihui, Yongxin Jin, Fang Bai, and Shouguang Jin. 2015. “Chapter 41 – Pseudomonas Aeruginosa.” In *Molecular Medical Microbiology*.

Yahr, Timothy L., Amy J. Vallis, Michael K. Hancock, Joseph T. Barbieri, and Dara W. Frank. 1998. “ExoY, an Adenylate Cyclase Secreted by the Pseudomonas Aeruginosa Type III System.” *Proceedings of the National Academy of Sciences of the United States of America*. https://doi.org/10.1073/pnas.95.23.13899.

Appendix A: Supplementary Information

A.1. Bacteria Quantification Assay

A.1.1. Methods

An mOrange filter was used to visualize *P. aeruginosa* strain PA14 mKO. A control experiment was first performed in which PA14 cells were seeded on a glass slide and several snapshots were taken using the fluorescent filter. ImageJ was subsequently used to obtain an average area per bacterium of 1.6 μm^2. Next, a typical invasion assay was performed in which PA14 bacteria were introduced to the seeded fibroblast and fluorescent images were taken every 15 minutes (Figure A.1). Each fluorescent frame prior to cell death was analyzed by obtaining the total area for fluorescent signal on the cell body and dividing it by the average area per bacterium, resulting in the number of bacteria attached to a fibroblast.

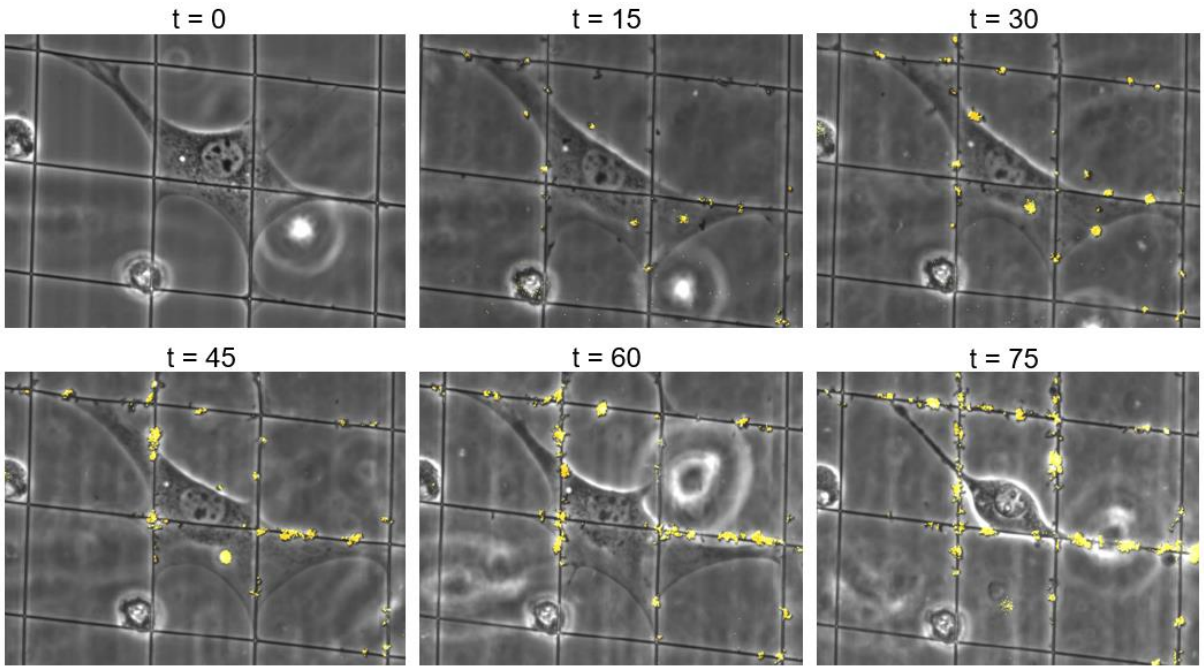

Figure A.1. Composite bright-field and fluorescent time-lapse microscopy images of *P. aeruginosa* (yellow) invasion in fibroblast cells on a 50 µm spaced polystyrene fiber mesh.

A.1.2. Results

The number of bacteria attached to each fibroblast was counted every 15 minutes to gauge if attachment number had any effect on the mode of death (sharp vs. gradual) or force exertion. Results demonstrated no time dependent change on number of attached bacteria to most fibroblasts analyzed, as the attachment number stayed fairly consistent throughout time (Figure A.2). However, *P. aeruginosa* quickly clumped as they grew in the nutrient rich cell media, making it hard to count the number of bacteria in each three-dimensional clump. In addition, it was difficult to determine if bacteria were attached to protrusions splayed out on the fiber networks, or if they were just attached to the fibronectin coated fibers. It was also determined that since *P. aeruginosa* strain PA14 has a mutation in the contact dependent T3SS and strain PAO1 has increased activity of the contact dependent T6SS, counting bacteria attachment number for PA14 exposed cells may not be a relevant parameter for investigation (Mikkelsen, McMullan, and Filloux 2011; Thibault G. Sana et al. 2015).

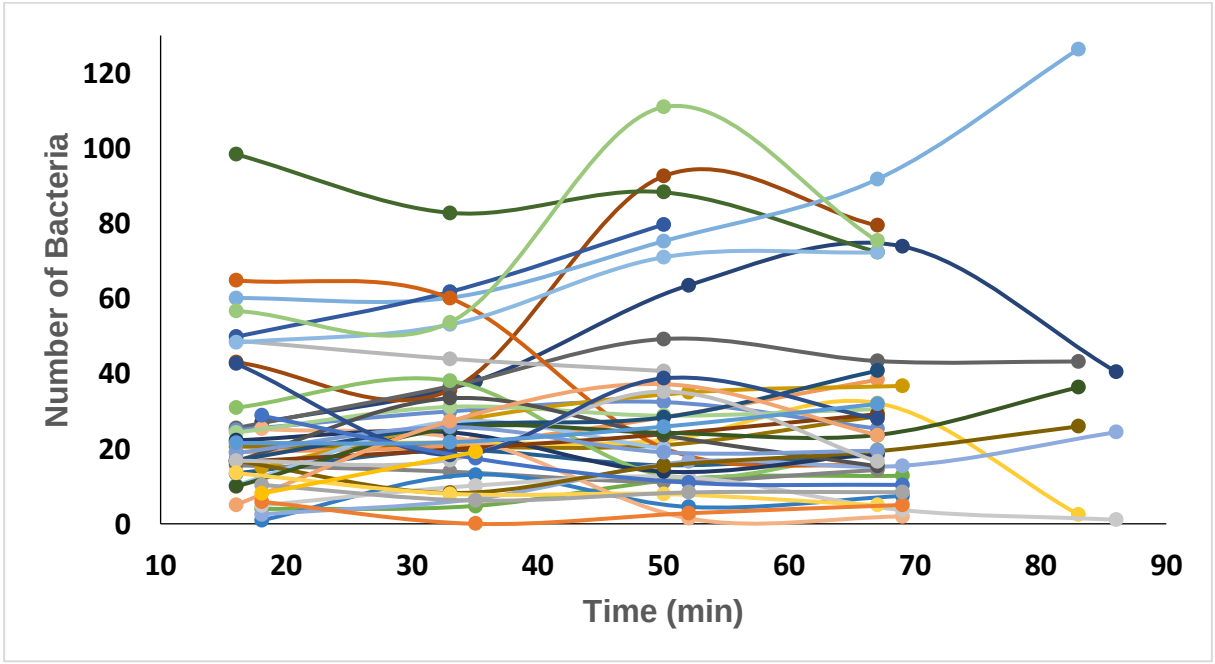

Figure A.2. The number of bacteria attached to each fibroblast was quantified at various points throughout invasion.

A.2. Sharp and Gradual Time of Death

Table A.2.1. Average time of death levels of significance for cells of all morphologies exposed to PA14 dying by sharp and gradual shape changes to death.

Morphology	Level		Average Time of Death (min)
50 μm Sharp	A		118
20 μm Sharp	A		117
Parallel (25) Sharp	A		115
50 μm Gradual	A		114
5 μm Sharp	A		112
Parallel (15) Sharp	A		111
20 μm Gradual	A	B	109
Parallel (15) Gradual	A	B	106
Parallel (25) Gradual	A	B	106
Flat Gradual	A	B	104
5 μm Gradual	A	B	102
Flat Sharp		B	89

Table A.2.2. Average time of death levels of significance for cells of all morphologies exposed to PAO1 dying by gradual shape change to death.

Morphology	Level	Average Time of Death (min)
20 μm Gradual	A	277
5 μm Gradual	A	270
50 μm Gradual	A	265
Flat Gradual	A	261
Parallel (25) Gradual	A	258
Parallel (15) Gradual	A	249